Thesis for the degree
Master of Science

Submitted to the Scientific Council of the
Weizmann Institute of Science
Rehovot, Israel

עבודת גמר (תזה) לתואר
מוסמך למדעים

מוגשת למועצה המדעית של
מכון ויצמן למדע
רחובות, ישראל

By
Yehonatan Dallal

מאת
יהונתן דלאל

לקראת שער באמינות גבוהה על סיבית קוונטית של יון לכוד
Towards High Fidelity Single Ion Qubit Gate

Advisor:
Dr. Roee Ozeri

מנחה:
ד"ר רועי עוזרי

February, 2009

שבט, תשס"ט

Abstract

Fault tolerant quantum error-correction schemes require the implementation of high fidelity quantum gates. The fidelity of a quantum gate is defined as the probability of being in the target final state $|\psi\rangle$, following the gate, $F = \langle \psi | \hat{\rho}_{final} | \psi \rangle$ where $\hat{\rho}_{final}$ is the density operator of the real final (mixed) state. We designed and built a system that will implement high fidelity stimulated Raman gates on single trapped ion-qubits. Our qubit levels are the two Zeeman states of the electronic ground level of a $^{88}Sr^{+}$ ion, separated by 2.8 MHz/G . Raman beams are generated by an External Cavity Diode Laser, where the Laser diode used is a violet LD of 405 nm, off-resonance with the transitions to levels at 422 nm and 408 nm. The two, co-propagating, Raman beams are the two polarization components of the 405 nm light where one polarization component is phase modulated at the qubit Level separation by an (electro optic modulator) EOM. The Rabi frequency is directly monitored by mixing down the beat-note of the two Raman beams and actively stabilized using feedback control. A Field Programmable Gate Array card is used to implement the control electronics with the advantage of flexibility and better integration with the experiment. Classical noises are suppressed such that the expected error ($\varepsilon = 1 - F$) is quantum limited due to spontaneous scattering of photons and smaller than 10^{-4}.

Dedication

To Gali, my wife, without your love and patience I would never have reached this point.

To Noga, my beautiful daughter, who had her first birthday just few days ago, and whose laughter makes me go home sooner than expected.

Thank you both for helping me remember what is really important in life.

Acknowledgments

I would like to thank Dr. Roee Ozeri, a great teacher and true optimist, who taught me much of what I know of laboratory work and whose love for physics is truly inspiring. Thanks to Yinnon Glickman, Nitzan Akerman and Shlomi Kotler for lending me a helping hand with so many collimations and calculations.

Contents

List of Figures

Preface

This thesis describes my work over the past year. I have designed and built a laser system that will be used to perform single qubit gates on a trapped ion qubit with high fidelity. The classical contribution to the errors in the gate is estimated to be $\varepsilon_c < 10^{-7}$. The gate be therefore quantum noise limited, i.e. limited by the spontaneous scattering of photons from the ion with $\varepsilon_s = 8 \times 10^{-6}$. The classical noises have been attenuated by active feedback methods. The laser was not tested on the ion since the state detection scheme was not yet fully implemented in the lab by the time this thesis was written, but experiments demonstrating gate fidelity higher than $1 - 10^{-4}$, a threshold level for fault tolerant quantum error processing are planned for the following months.

1 Quantum information processing

Since the middle of the last century, continuous technological and scientific progress has pushed the limits of computer technology to produce faster and smaller processors. Today's state of the art processors have fundamental processing units (transistors) of the size of 45 nm. Current road-map for the semiconductor industry shows planned transition to a 11 nm manufacturing process by the year 2022[1]. This amazing progress was foreseen by Intel's co-founder Gordon Moore in 1965 when he predicted that the density of transistors on a chip will double itself every two years. However, this progress will eventually run itself down. The size of the fundamental computing units is bound to reach atomic sizes. At the atomic scale the behavior of systems is not necessarily classical but rather can be governed by the laws of quantum mechanics. As an example, the measurement of a memory bit state will no longer be predicted deterministically. It is only the probability of different outcomes, determined by their respective quantum amplitudes can be known. The usual paradigm of computers, namely the Turing Machine, can no longer be realized on such physical systems. Quantum effects also holds the promise for a new kind of computer- the quantum computer, a system that performs computations by using quantum mechanical principles for it's operations. As was pointed out by Richard Feynman in 1982, a full simulation of a large (more than a few degrees of freedom) quantum mechanical system is inefficient on a classical computer, but trivial on a quantum computer [1, 2]. At first these ideas were mainly a source of theoretical discussions, but then it was discovered that utilizing the inherent parallelism of the quantum superposition principle,

[1] `http://www.itrs.net/Links/2008ITRS/Update/2008_Update.pdf`
`http://en.wikipedia.org/wiki/11_nanometer`

solutions to problems that are considered unsolvable in classical computer science (or at least too time consuming) can obtained. One major breakthrough by Shor's factoring algorithm demonstrating [3, 4] that a quantum computer should be able to efficiently factor large numbers to their prime constituents. If ever implemented it will have a profound effect on cryptography, as it would render current methods for public key encryption (such as RSA) obsolete.

Current research in the field of quantum information and quantum computers attempts to find solutions to a number of basic problems, such as scalability (how to build quantum computers of many degrees of freedom), decoherence (attempt to overcome decoherence hindering the performance of quantum computers by loss of information), quantum algorithms (what kind of computations can be done with a quantum computer) and communication (transferring information between quantum computers). This thesis deals with only one simple building block of a quantum computer: the coherent control of the state of a single quantum bit (qubit) without loss of information in the process.

1.1 Qubits

The basic building blocks of classical computers are bits (binary-digits). Bits can assume one of two logical values usually denoted as 0 and 1. An array of several bits (a register) can represent 2^N different numbers or states. In contrast, qubit is a quantum two level system. Qubits have 2 well defined states, similarly to the classical bits, but due to the principle of quantum superposition, they can be in any superposition state $|\psi\rangle = \alpha|0\rangle + \beta|1\rangle$. A quantum register of N qubits spans a 2^N dimensional Hilbert space, meaning that we need 2^N complex numbers to fully specify a state. This is in sharp contrast with the classical case where only N numbers are needed to specify an N bit state. It is customary to represent the state of a single qubit as a vector pointing on the surface of a unity sphere - the Bloch sphere. Since qubit states are normalized to unity we can write without loss of generality $|\psi\rangle = \cos(\theta/2)|0\rangle + e^{i\phi}\sin(\theta/2)|1\rangle$. The angles θ, ϕ define the direction of the qubit vector. In this notation the $|0\rangle$ ($|1\rangle$) (also referred to as $|\downarrow\rangle$ and $|\uparrow\rangle$) state is represented by a vector pointing in the south (north) pole direction. Equal superpositions ($|\alpha|^2 = |\beta|^2 = \frac{1}{2}$) are vectors lying on the Bloch sphere equatorial plane.

1.2 Quantum Gates

Large classical computations can be carried out using only one and two-bit gates. There is only one possible classical single bit gate: the NOT gate. The NOT gate flips the state of the bit from 1 to 0 and vice-versa. There are many different two-bit gates. Examples include the OR gate, the NAND gate and

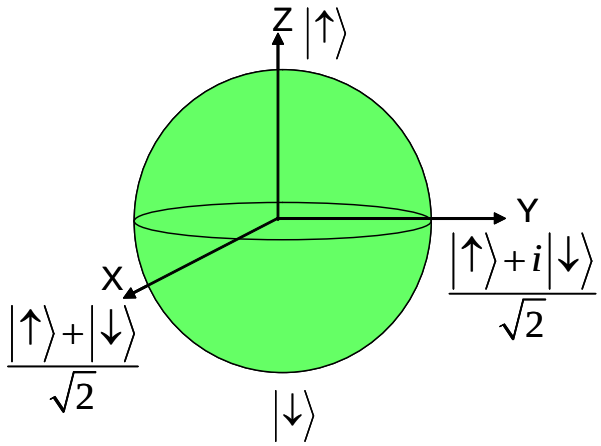

Figure 1: The Bloch Sphere

the AND gate with truth tables given in table 1. An important theoretical result states that any binary function (the result of which is 0 or 1) of bits can be computed by a composition of NAND gates alone. Therefore the NAND gate is a universal gate - any other gate can be decomposed into NAND gates [1].

A	B	out
0	0	0
1	0	1
0	1	1
1	1	1

(a) OR

A	B	out
0	0	0
1	0	0
0	1	0
1	1	1

(b) AND

A	B	out
0	0	1
1	0	1
0	1	1
1	1	0

(c) NAND

Table 1: OR,AND,NAND classical gates

Quantum computation also uses single and multiple qubit gates. The QNOT, the quantum analogue of the classical NOT, is a gate that flips the state of the qubit: $\alpha|0\rangle+\beta|1\rangle \longrightarrow \alpha|1\rangle+\beta|0\rangle$. the simple QNOT gate can be generalized to a rotation operator in the Bloch sphere, that operates on the spinor $\begin{pmatrix}\alpha\\ \beta\end{pmatrix}$,

$$\hat{R}(\theta,\phi)=\begin{pmatrix}\cos(\theta/2) & -ie^{-i\phi}\sin(\theta/2)\\ -ie^{-i\phi}\sin(\theta/2) & \cos(\theta/2)\end{pmatrix},$$

where QNOT gate is $\hat{R}(\theta=\pi,\phi=0)$. The rotation operator can be represented in terms of the Pauli matrices $\hat{R}(\theta,\phi)=e^{\frac{-i\sigma\cdot\hat{\mathbf{n}}\theta}{2}}$ where σ is the Pauli vector $(\sigma_x,\sigma_y,\sigma_z)$ and $\hat{\mathbf{n}}$ is a unit vector in the Bloch sphere equatorial plane. Physically the angles θ and ϕ are determined by the strength and phase of the interaction with the qubit, respectively. The main goal of this work is to implement such a single qubit gate that will perform with a fidelity (defined in subsection 1.3) better than $1-10^{-4}$. Rotations around

the $\hat{x}$ ($\hat{y}$) axis in the Bloch sphere correspond to $\phi = 0\,(\frac{\pi}{2})$. Quantum gates involving two qubits also exist but are outside the scope of this thesis. I will only mention the quantum controlled NOT gate (CNOT) where the state of the target qubit is flipped conditioned on the control qubit state: $|00\rangle \rightarrow |00\rangle, |01\rangle \rightarrow |01\rangle, |10\rangle \rightarrow |11\rangle, |11\rangle \rightarrow |10\rangle$ here the first is the control qubit and the second is the target qubit. It can be shown that any multiple qubit unitary operation can be composed of the CNOT together with the single rotations , hence they form a universal gate set, similarly to the classical NAND [5].

1.3 Gate Fidelity

The fidelity of a quantum gate can be defined as the probability of measuring the qubit in the ideal target state $|\psi\rangle$, $F = \langle \psi | \hat{\rho}_{final} | \psi \rangle$, and $\hat{\rho}_{final}$ is the actual density operator reached after the gate.

1.4 Fault Tolerance

Many computational algorithms rely on long sequences of gating operations. Suppose there is some error probability p in any single gate, the error in the result of a computation is $\varepsilon \approx 1-(1-p)^N$ where N is the number of gates in the computation. The exponential dependence of the error on N prohibits large scale computation. Noise is a fact of life and cannot be completely eliminated. Classical information can be protected against the affect of noise by encoding it to "error correction codes" that are noise resilient. These codes are usually met in the context of communication over noisy channels rather than in computation, this is due to the fact that CMOS technology which is at the heart of modern processors is very reliable, and errors are rare, estimated at bellow one error in every 10^{17} operations (for a 3 GHz processor this is one error in 3 years of continuous operation). Quantum gates with such low noise are probably not feasible even theoretically, due to quantum fluctuations. But we can use quantum error correction to protect states and improve the fidelity of gates. Remarkably, it turns out that quantum computation with an arbitrary low error can be achieved even with noisy gates, using certain error-correction schemes and provided that the single gate error is bellow a certain threshold [1]. These ideas are reminiscent of the Shannon noisy channel coding theorem that states that classical information can be sent over a noisy channel with arbitrary low error rate provided that a strong enough coding scheme is used [6]. In order to theoretically estimate the threshold for fault tolerant QIP it is necessary to assume certain noise models, quantum error-correction protocols, architecture etc. These estimates are therefore only rough guidelines for the fidelities with which quantum gates should be realized in the lab. In the last few years fault tolerant error thresholds a high as 0.01 were calculated. It is believed however that

in order for fault tolerance to be experimentally feasible, quantum gates with significantly lower errors, such as 10^{-4}, should be realized.

1.5 Trapped Ion Qubits

The requirements for the implementation of a quantum information processor are nicely summarized by the five criteria by Divincenzo[7]:

1. The qubits must be well-defined.
2. It must be possible to initialize the qubit to a pure state.
3. A universal set of quantum gates must be implemented.
4. Qubit specific measurements must be implemented.
5. Coherence times must be long with respect to gating and measurement times.

Among many systems considered as a physical qubit, cold trapped ions has all those features. Trapped ions are well isolated from their environment, hence long coherence times are possible. The internal degrees of freedom of trapped ions are easily initialized using optical pumping methods and are easily manipulated by laser or microwave radiation. It is possible to detect their state using fluorescence spectroscopy methods. Hence cold trapped ions are considered as promising candidates for the implementation of quantum computing, and all of Divincenzo's criteria, high fidelity gates [8], initialization and readout [9, 10], long coherence times [11] and entanglement gate [12] has been demonstrated with trapped ions.

2 The $^{88}Sr^{+}$ Qubit

Strontium is an alkaline earth metal with 2 electrons in its valance orbital. We use ^{88}Sr which is the most abundant isotope of strontium (82% natural abundance). The singly ionized strontium ion has only one electron in its valance orbital, $5S_{\frac{1}{2}}$, hence it resembles an alkali atom. $^{88}Sr^{+}$ has no nuclear spin (it has 38 protons and 50 neutrons) and hence no hyperfine structure. The electronic ground state is therefore only twice degenerate and is Zeeman splitted with 2.8 MHz/G. We use the two Zeeman splitted spin states of the ground level to encode a physical qubit. Figure 2 presents a diagram of the relevant energy levels of $^{88}Sr^{+}$.

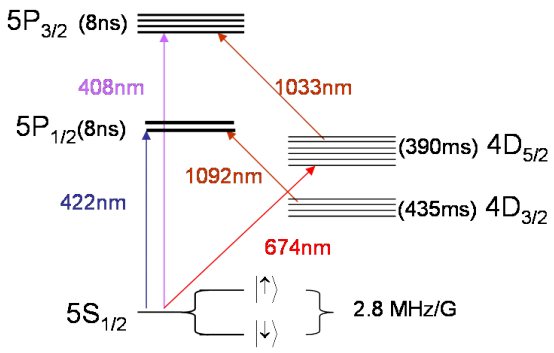

Figure 2: Relevant $^{88}Sr^{+}$ energy levels

transition wavelengths. Level lifetimes are given in parentheses.

2.1 Trapping

Applying forces on charged particles, is possible using electrostatic fields. However, a simple electrostatic trapping device is not possible as a consequence of the Laplace equation: $\nabla^2\phi = \left(\frac{\partial^2}{\partial x^2} + \frac{\partial^2}{\partial y^2} + \frac{\partial^2}{\partial z^2}\right)\phi = 0$. If a trapping minimum of the potential exists in 2 directions there must be an anti-trapping maximum in the third. The solution is to use time dependent fields to achieve an effective trapping potential. In our experiments we use the "Linear RF-Paul Trap" invented by Wolfgang Paul [13]. Figure 3 shows the configuration of a basic Paul trap. The ion is captured in the trapping region between the "end caps" which are DC electrodes, held at RF ground. Two other electrodes are connected to a sinusoidal varying voltage, typically of few hundred volts of amplitude. The other 2 electrodes are grounded. At each instant of time the trap potential is an electric quadrupole; radially confining in one direction and anti-confining in the other. However, with the correct choice of parameters, the ion can't follow fast enough and remains essentially at the center of the trap. A full treatment of the motion of the ion in the trap, both classical and quantum, is given in references [14, 15]. An important result on cited here states the trapping potential can be approximated as a simple harmonic potential, and that the motion of the ion in trap can be treated as that of a quantum harmonic oscillator.

2.2 Laser cooling

The trapped ions are initially hot ($\approx 600\,\mathrm{K}$) as they are emitted from a hot oven. The trap is deep enough to capture them ($\approx 1\,\mathrm{eV} = 20\,k_B T$) but due to a Doppler broadening much wider than the qubit separation they are useless as qubits, unless cooled. In order to cool the ions the method of Doppler laser cooling is used. In the context of a single trapped ion "cooling" does not imply that the trapped ion is brought to

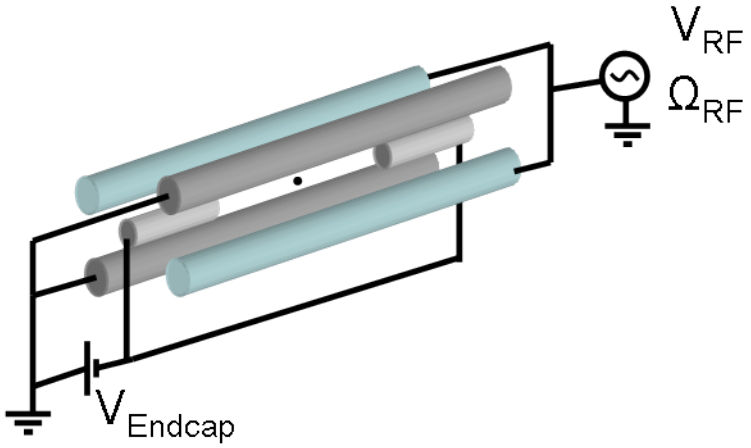

Figure 3: Schematic of a Paul Trap.
End-cap electrodes are held at a DC potential V_{endcap} and define the longitudinal axis of the trap. The two RF electrodes (blue rods) are connected to a radio frequency potential of amplitude V_{RF} and frequency Ω_{RF}. The other 2 electrodes (gray rods) are held at RF ground.

thermal equilibrium with a reservoir [16]. However, using ergodicity the ion's average occupation of the harmonic oscillator states over many cooling repetitions follows a Boltzmann distribution thus defining a measure of temperature. After Doppler cooling on the $S_{\frac{1}{2}} \rightarrow P_{\frac{1}{2}}$ transition down to the Doppler cooling limit of $T_d = \frac{\hbar\gamma}{2k_B} = 5 \times 10^{-4}\,\text{K}$, with a trap frequency of 2 MHz, the average occupation of the quantum harmonic oscillator is $\langle n \rangle \approx 10$. One interesting aspect of cooling a strongly trapped ion, in contrast with the cooling of weakly trapped particles is that since the ion is trapped, a single laser beam is enough for cooling in 3D and no elaborate configuration of the cooling beams is needed. As long as $\vec{k}$, the wave-vector of the laser has a projection along each of the axes of the trap (i.e. is not parallel to any of the axes), the ion will spend some of the time moving towards the laser and will therefore be cooled [17]. For this cooling scheme to work the trap cannot be isotropic, and needs to have 3 different non-degenerate axes.

2.3 Re-pumping

The excited state $5P_{\frac{1}{2}}$ has some probability to spontaneously decay to the metastable state $4D_{\frac{3}{2}}$. Similarly $5P_{\frac{3}{2}}$ level can decay to either of the D states, $4D_{\frac{3}{2}}$ and $4D_{\frac{5}{2}}$. The branching ratio for these decays into D is about $1/14$ of the total decay rate [18]. Because the D states are metastable with lifetimes on the order of 0.5 sec the cooling process is practically terminated when such decay occurs. This means that during cooling or fluorescence detection, the ion may suddenly become "dark" and cease to interact with the laser field. Since on the average this happens once in every 14 scattering events, and given the

short lifetimes of the P levels ($\tau = \frac{1}{\gamma} \approx 8\,\text{ns}$) cooling sequences longer than few hundred nano-seconds are not possible. In order to be able to cool or perform fluorescence detection, the population must be re-pumped out of the D states. This is done with a laser beam of 1092 nm (1033 nm) resonant with the $4D_{\frac{3}{2}} \rightarrow 5P_{\frac{1}{2}}$ ($4D_{\frac{5}{2}} \rightarrow 5P_{\frac{3}{2}}$) transition. A numerical solution of the optical Bloch equations gives the steady state populations of the different levels ($5\mathrm{S}_{\frac{1}{2}}, 5\mathrm{P}_{\frac{1}{2}}$ and $4\mathrm{D}_{\frac{3}{2}}$) for different magnetic field strengths and for different intensities and detuning of the 422 nm and 1092 nm lasers.

2.4 Qubit states

A constant magnetic field splits the $5\mathrm{S}_{\frac{1}{2}}$ level into two spin states. The state with electronic spin parallel (anti-parallel) to the externally applied magnetic field is denoted ($|\uparrow\rangle$) $|\downarrow\rangle$. One disadvantage in using Zeeman states as qubit levels is that fluctuations of the quantizing magnetic field will cause fluctuations in the Zeeman separation between the qubit levels therefore dephasing superpositions. To reduce the affect of magnetic noise dephasing we use servo stabilization of the magnetic field. Noises in the magnetic field has been brought down to a level of $1\,\mu$G at 50 Hz, the dominant spectral component of magnetic field noise.

2.5 State detection

The general state of the ion qubit can be written as $|\psi\rangle = \cos\frac{\theta}{2}|\uparrow\rangle + \sin\frac{\theta}{2}e^{i\phi}|\downarrow\rangle$. Internal state detection in trapped ions is typically done by state selective fluorescence. Here photons are scattered from a laser beam only if the ion is in one of the qubit levels and the other qubit level is "dark". In the case where the Zeeman splitting between the qubit levels is small compared with the natural width of the $P_{\frac{1}{2}}$ and the $P_{\frac{3}{2}}$ levels, simple state selective fluorescence will not work as both qubit levels will be simultaneously on resonance. Therefore we use the method of electron shelving: detection of the state of the ion is done in two stages. First a 674 nm laser with a line-width narrower than the qubit level separation is used to coherently transfer population from the $|\uparrow\rangle$ state to the metastable (with lifetime of 0.4 sec) $4D_{\frac{5}{2}}$ state. Then a laser beam on-resonance with the $S_{\frac{1}{2}} \leftrightarrow P_{\frac{1}{2}}$ transition (422 nm) is turned on. If the ion-qubit superposition collapses to the $|\downarrow\rangle$ state, photons are scattered on the ($S_{\frac{1}{2}} \leftrightarrow P_{\frac{1}{2}}$) transition and are collected on a photo-multiplier tube. While if the ion superposition collapses to the $4D_{\frac{5}{2}}$ level then no photons are detected. The scattered photons are detected by a photo-multiplier-tube (PMT) and counted. If the number of scattered photons detected is larger than a threshold determined by the background photon rate then the recorded result of the measurement is $|\downarrow\rangle$ and otherwise it is $|\uparrow\rangle$. Each measurement

is repeated many times to gain statistics [10]. The above detection scheme only provides us with the probability of finding a superposition in $|\uparrow\rangle$ or $|\downarrow\rangle$ states - the projection of the Bloch vector state on the $\hat{z}$ axis of the Bloch sphere . To measure the projections along $\hat{x}$ ($\hat{y}$) a $\theta = \frac{\pi}{2}$ pulse with $\phi = 0$ ($\phi = \frac{\pi}{2}$) is applied prior to measurement. This pulse rotates the Bloch vector so $\hat{x}$ ($\hat{y}$) component is now along $\hat{z}$, and can be measured. Quantum state tomography uses measurements of the projection of identical copies of a quantum state along three orthogonal directions to determine the direction of the Bloch vector on the Bloch sphere, limited by statistics and the fidelity of the detection and the single qubit gates.

2.6 Trapped ion - light interaction

The interaction between an ion and an electric field of a laser can be written as [19]:

$$H_I = -\mathbf{d} \cdot E_0 \hat{\varepsilon}_L \cos(\mathbf{k}\tilde{z} - \omega_L t + \phi), \tag{1}$$

where $\mathbf{d}$ is the electric dipole operator, E_0 is the electric field amplitude, $\hat{\varepsilon}_L$ is the laser polarization vector, $\mathbf{k}$ is the laser k-vector assumed parallel to the trap axis and $\tilde{z}$ is the ion position operator. Here we the ion is assume a two level system, a reasonable approximation as long as the field is only resonant with one transition of the ion and that the Rabi frequency is much smaller than the detuning to off-resonant transitions. We define the Lamb-Dicke parameter $\eta = kz_0$ where $z_0 = \sqrt{\frac{\hbar}{2m\omega}}$ is the extent of the ion ground state wavefunction. In the Lamb-Dicke regime, where $\left\langle (\hat{a}^\dagger + \hat{a})^2 \right\rangle \eta^2 \ll 1$, achieved by tight trapping and cooling, the interaction Hamiltonian can be approximated by

$$H_{int} = \hbar(\Omega e^{i\phi})\sigma^+ e^{-i(\omega_L - \omega_0)t}[1 + i\eta(ae^{-i\omega_z t} + a^\dagger e^{-\omega_z t})] + h.c. \tag{2}$$

where $\hbar\omega_0$ is the energy separation between the two levels, $\Omega = -E_0 \langle\uparrow | \mathbf{d} \cdot \hat{\varepsilon}_\mathbf{L} | \downarrow\rangle / (2\hbar)$ is the on-resonance Rabi frequency, $\sigma^+ = |\uparrow\rangle\langle\downarrow|$ is a raising operator for the internal state and $a^\dagger$ is a creation operator for the quantum harmonic oscillator. For the case of Raman transitions induced by two beams with frequencies $\omega_{1,2}$, we can replace $\omega_L \to \Delta\omega = \omega_1 - \omega_2$, $k \to \Delta k = k_1 - k_2$ [19]. For certain choices of $\Delta\omega$ the interaction is resonant. For example, for the case where $\Delta\omega = \omega_0 + m\omega_z$ a transition $|\downarrow\rangle|n\rangle \rightleftarrows |\uparrow\rangle|n+m\rangle$ is induced. In this thesis we focus on carrier transitions where $\Delta\omega = \omega_0$ and $\eta = 0$. The condition on η is fullfiled almost exactly since co-propagating beams are used and therefore $\Delta k \cong 0$.

2.7 Manipulation of the ion qubit state

Manipulation of the ion internal state can be implemented by the use of an electro magnetic field. In the case where the levels of interest are Zeeman splitted spin states of the valance electron, typical level separation is of the order of a few MHz (2.8 MHz/G). As the spin is a magnetic dipole, a magnetic field, perpendicular to the quantization axis and oscillating at the qubit level separation (RF frequency) will induce spin rotations. However - the long wavelength of such low frequency fields (100 m at 3 MHz) prohibits single ions addressing. Furthermore, two ion gates require coupling to the motional degrees of freedom of the trapped ions [19, 20]. This cannot be done using RF fields alone since the Lamb-Dicke parameter kz_0 will be essentially zero. An alternative method to couple between the qubit states is indirect - a laser field is used as a carrier for the RF frequency via two-photon transitions. The short wavelength of the laser enables single ion addressing and the larger wave-vector allows for a large Lamb-Dicke parameter, required for coupling to motional degrees of freedom. The laser is modulated at the RF frequency and sidebands are created. The ion then undergoes stimulated Raman[2] transitions where it absorbs a photon from one sideband and coherently emits it into the other sideband. For a detailed analysis of this two-photon process see [21, 10]. The ion is modeled as a three level Λ system and two light fields act on it with a frequency separation matching the separation between the two lower levels. The third, excited level is removed from the coupled equations by the process of adiabatic elimination. In a frame rotating at the frequency separation between the fields, the interaction Hamiltonian finally takes the form (within the rotating wave approximation)

$$H_I = \frac{\hbar\Omega_R}{2}\left|\uparrow\right\rangle\left\langle\downarrow\right| + \frac{\hbar\Omega_R^*}{2}\left|\downarrow\right\rangle\left\langle\uparrow\right| = \frac{\hbar}{2}\begin{pmatrix} 0 & \Omega_R \\ \Omega_R^* & 0 \end{pmatrix}, \tag{3}$$

with a Rabi frequency Ω_R that depends on the two fields. This is the same as the Hamiltonian in Eq. (2) a for carrier transition, i.e. $\Delta n = 0$. The Rabi frequency is calculated in the following subsection 2.7.1.

2.7.1 Calculation of the Raman transition Rabi frequency

Raman transition is a two photon process where a photon from one mode of the field is scattered into another mode of the field. The difference in energy is transferred to the valance electron. Stimulated

[2] Sir Chandrasekhara Venkata Raman (7 November 1888 – 21 November 1970) was an Indian physicist who was awarded the 1930 Nobel Prize in Physics for his work on the molecular scattering of light and for the discovery of the Raman effect, which is named after him. (from wikipedia.com)

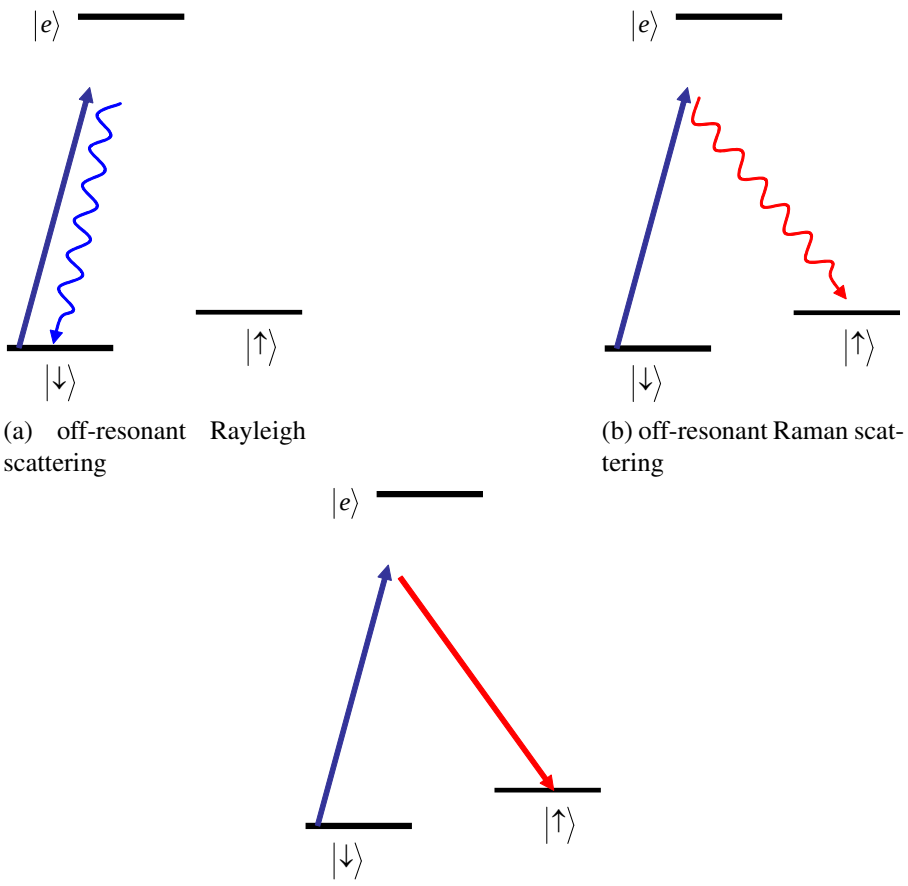

(a) off-resonant Rayleigh scattering

(b) off-resonant Raman scattering

(c) Raman stimulated transition

Figure 4: off-resonant Raman transition and scattering and Rayleigh scattering

Raman transitions are the coherent counterpart of this two photon process. Since there is macroscopic occupation of two modes of the field, scattering from one mode into the other is preferred by bosonic amplification. The ion then coherently scatters photons from one mode to the other and gains/loses the difference between the modes in momentum and energy. The end result is Rabi nutation of the internal state of the trapped ion induced by the Raman field. The Rabi frequency of the Raman carrier transition is given by [19]

$$\Omega_R = \frac{e^{i\Delta\phi}}{4\hbar^2}\sum_i \frac{\langle\uparrow|\mathbf{d}\cdot E_2\hat{\varepsilon}_2|i\rangle\langle i|\mathbf{d}\cdot E_1\hat{\varepsilon}_1|\downarrow\rangle}{\Delta_i}, \tag{4}$$

where $|i\rangle$ are the virtually excited intermediate states of the Raman transition, $\Delta\phi$ is the phase difference between the two Raman beams, $\mathbf{d}$ is the dipole operator of the ion, E_j is the j'th beam electric field amplitude and $\hat{\varepsilon}_j$ is its polarization. The laser detuning from the transition to level $|i\rangle$, is given by Δ_i and $\hbar$ is Planck's constant . In this expression it is assumed that $\Delta_i \gg \gamma_i$, i.e. the detunings are much larger than the line-widths of the intermediate levels. The transition of interest is between the Zeeman levels of

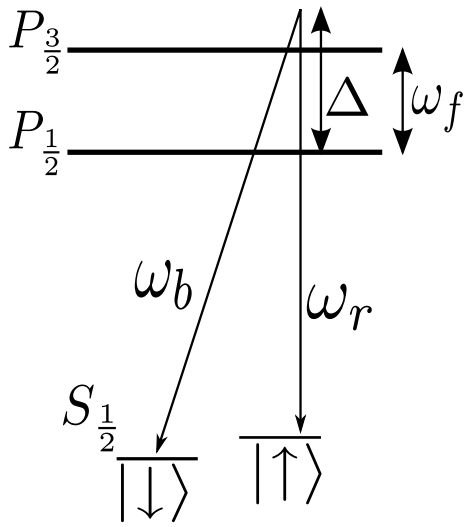

Figure 5: Relevant energy levels for stimulated Raman transitions

the $5S_{\frac{1}{2}}$ state. The laser used is at approximately 405.5 nm. In this case the only relevant intermediate states are the Zeeman levels of the $5P_{\frac{1}{2}}$ and the $5P_{\frac{3}{2}}$. Let us look on the transition between $|\downarrow\rangle$ and $|\uparrow\rangle$ (the $m = \pm\frac{1}{2}$ levels of the $5S_{\frac{1}{2}}$ state, respectively). To make this transition the valance electron has to gain energy, so the emitted photon must be red w.r.t. the absorbed photon. Raman transitions between $|\uparrow\rangle$ and $|\downarrow\rangle$ require two beams with a frequency difference that matches the qubit level separation. In the notation of Eq. (4) beam 1 has the higher frequency, i.e. $E_1 = E_b$ (blue beam) and $E_2 = E_r$ (red beam). Both beams can be decomposed to their different polarization components. We therefore write $E_1\hat{\varepsilon}_1 \rightarrow E_b\hat{\varepsilon}_b = E_b\left(b_{\text{-}}\hat{\sigma}_{\text{-}} + b_0\hat{\pi} + b_+\hat{\sigma}_+\right)$ ("blue beam") and $E_2\hat{\varepsilon}_2 \rightarrow E_r\hat{\varepsilon}_r = E_r\left(r_{\text{-}}\hat{\sigma}_{\text{-}} + r_0\hat{\pi} + r_+\hat{\sigma}_+\right)$ ("red beam") in (4). Rewriting Eq. (4) more specifically for the atomic energy levels involved we have

$$\Omega_R = \frac{e^{i\Delta\phi}}{4\hbar^2}\sum_{J=\frac{1}{2},\frac{3}{2}}\sum_{m=-J}^{m=J}\frac{\langle\uparrow|\mathbf{d}\cdot E_r\hat{\varepsilon}_r|5P_J,m\rangle\langle 5P_J,m|\mathbf{d}\cdot E_b\hat{\varepsilon}_b|\downarrow\rangle}{\Delta_{J,m}} \tag{5}$$

the sum is a coherent addition of the processes described graphically in figure 6. The matrix elements in (5) are evaluated with the Wigner-Eckart theorem, for details see A.1 in the appendix [22, 23]. We define the reduced matrix element $\mu = |\langle J'\|er\|J\rangle| = \sqrt{3\pi\varepsilon_0\hbar\frac{c^3}{\omega_0^3}\gamma}$ and the coupling constants $g_{b,r} = \frac{\mu E_{b,r}}{2\hbar}$. With

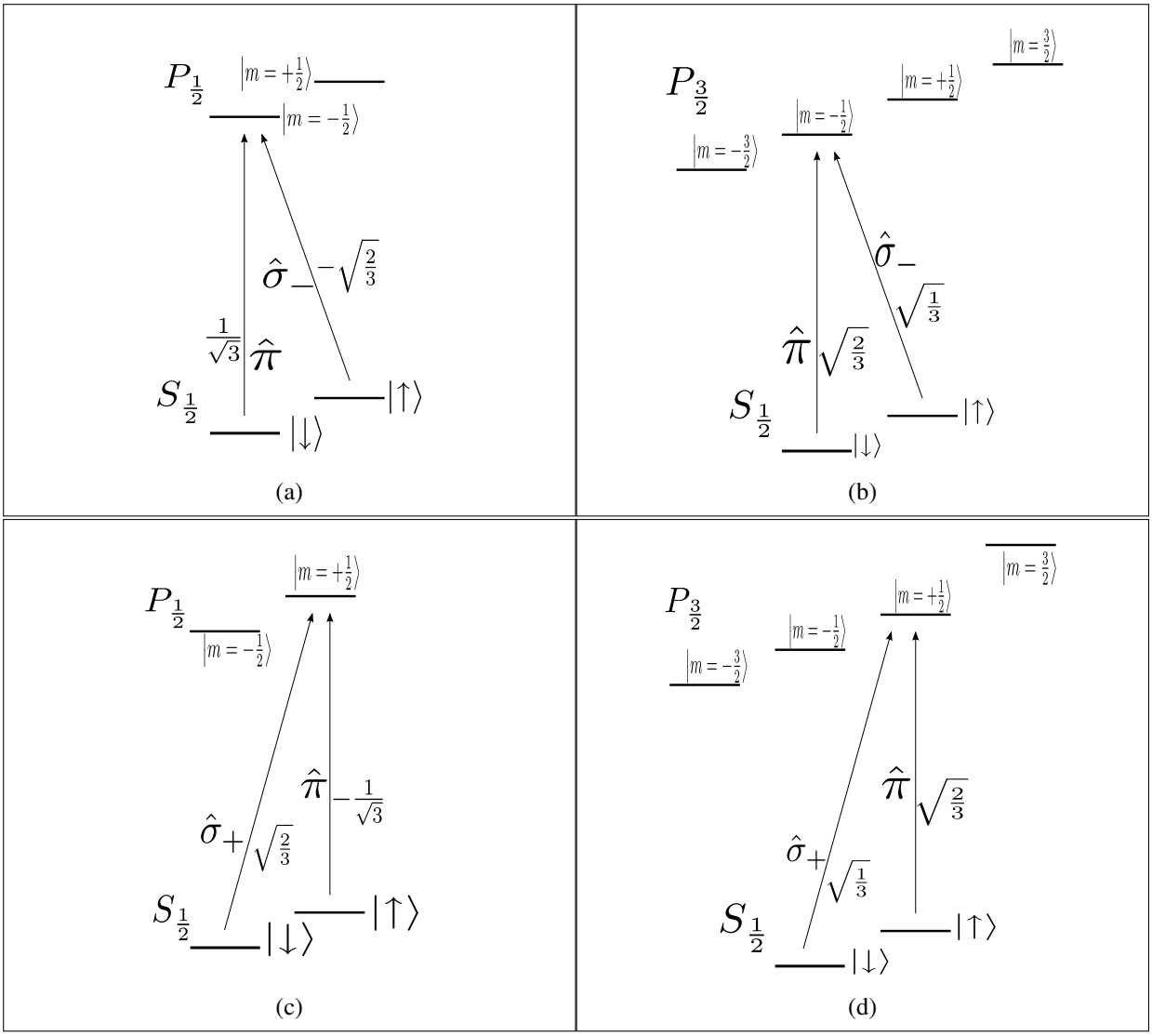

Figure 6: Clebsh-Gordan coefficient for relevant transitions

these we get the Rabi frequency (taking $\omega_{S_{1/2}\to P_{3/2}} \approx \omega_{S_{1/2}\to P_{1/2}} = \omega_0$ in μ)

$$\Omega_R = \\ = e^{i\Delta\phi} g_b g_r \left[b_0 r_- \frac{\sqrt{\frac{1}{3}}\left(-\sqrt{\frac{2}{3}}\right)}{\Delta} + b_+ r_0 \frac{\sqrt{\frac{2}{3}}\left(-\sqrt{\frac{1}{3}}\right)}{\Delta} + b_0 r_- \frac{\sqrt{\frac{1}{3}}\sqrt{\frac{2}{3}}}{\Delta-\omega_f} + b_+ r_0 \frac{\sqrt{\frac{2}{3}}\sqrt{\frac{1}{3}}}{\Delta-\omega_f} \right] = \\ = -e^{i\Delta\phi} \frac{\sqrt{2}}{3} g_b g_r \left(b_0 r_- + b_+ r_0\right) \frac{\omega_f}{\Delta\left(\Delta-\omega_f\right)} \quad (6)$$

Assuming a Gaussian beam with waist w_0 and using the relation $E^2 = \frac{4}{\varepsilon_0 c}\frac{P_0}{\pi w_0^2}$ we finally get the Rabi frequency in terms of available laser power, beam waist and the detuning from the $P_{\frac{3}{2}}$ energy level:

$$\Omega_R = -e^{i\Delta\phi}\sqrt{2}\frac{c^2}{\omega_0^3}\gamma\frac{1}{\hbar}\frac{P_0}{w_0^2}\left(b_0 r_- + b_+ r_0\right)\frac{\omega_f}{\Delta\left(\Delta-\omega_f\right)} \tag{7}$$

Using $P_0 = \hbar\omega_0\Gamma_{\mathrm{ph}}$ in Eq. (7) or $g^2 = 3\gamma\frac{\lambda^2}{(2\pi w_0)^2}\Gamma_{ph}$ in Eq. (6) we can write Ω_R in terms of the laser beam photon arrival rate Γ_{ph},

$$\Omega_R = -e^{i\Delta\phi}\sqrt{2}\gamma\frac{\lambda^2}{(2\pi w_0)^2}\Gamma_{ph}\frac{\omega_f}{\Delta\left(\Delta-\omega_f\right)}\left(b_0 r_- + b_+ r_0\right). \tag{8}$$

2.8 Decoherence

Decoherence of the ion qubit can occur during a gating operation or during storage. Here we refer to the former as "gating errors" and to the latter as "memory dephasing". Memory dephasing is mainly caused by fluctuations of the magnetic field. A detailed treatment of this effect can be found in [14]. The emphasis of this thesis is on minimizing gating errors. In his 1975 paper [24], Mollow showed that the effect of a coherent state field on an atom is equivalent to that of a classical field plus a quantum field initially in the vacuum state. Accordingly, the error in gating operations can be thought of as comprised of two parts - the fluctuations of the classical c-number (i.e. classical intensity and phase noises of the laser) and the second part that originates from the quantum nature of the electromagnetic field - i.e., the spontaneous scattering of photons [18]. An analysis of these two contribution follows.

2.8.1 Classical (technical) noises:

Technical noises are defined as all the noises present in the classical parameters of the laser interacting with the ion. These noises are ideally correlated between the ion and an independent measurement of the noisy parameter. Examples for this class of noises are fluctuations in the laser intensity resulting from e.g. unstable coupling to an optical fiber or a noisy drive current. In principle, since the noise in the Rabi frequency and that recorded on an independent detector are correlated, these noises can be compensated and effectively removed from the beam. An analysis of how these noises affect the fidelity follows.

Let us suppose that the gating operation is a simple rotation of the state vector with an angle θ_0 around the $\hat{x}$ axis of the Bloch sphere. An error in the amplitude of the Rabi frequency will result in an error in

the rotation angle: $\theta = \theta_0 + \Delta\theta$. The phase of the Rabi frequency, i.e. the direction of the Rabi vector in the equatorial plane is derived from the phase of the local RF oscillator that is assumed to be very stable. Hence errors in the phase, are expected to be small and are neglected. Phase errors due to an optical path difference are not an issue since the two Raman beams are co-propagating. The final state will therefore differ from the ideal target state and we write $\hat{\rho}_{final} = \left|\psi_{final}\right\rangle\left\langle\psi_{final}\right|$. The fidelity is

$$F = \left\langle\psi_{ideal}|\psi_{final}\right\rangle\left\langle\psi_{final}|\psi_{ideal}\right\rangle = \cos^2(\frac{\Delta\theta}{2}) \overset{\Delta\theta\ll\frac{\pi}{2}}{\longrightarrow} 1 - \frac{(\Delta\theta)^2}{4} \Longrightarrow \varepsilon_c = 1 - F = \left(\frac{\Delta\theta}{2}\right)^2$$

The error in the rotation angle is $\Delta\theta = \int_{-t_\pi/2}^{t_\pi/2} dt\Delta\Omega$. The mean square error (MSE) for the case where the correlation time for the noise, τ_c is much longer than the pulse duration, $\tau_c \gg t_\pi$, is $\left\langle\Delta\theta^2\right\rangle = t_\pi^2\left\langle\Delta\Omega^2\right\rangle$, since $\Delta\Omega(t)$ remains approximately constant within time t_π. This is simply the MSE of the Rabi frequency, multiplied by the square of the π time. The π time is inversely proportional to the Rabi frequency, $t_\pi = \frac{\pi}{2\Omega_R}$, so finally the classical errors are proportional to the relative noise of the Rabi frequency:

$$\varepsilon_{c,\pi} = \left(\frac{\pi}{4}\right)^2 \frac{\left\langle\Delta\Omega^2\right\rangle}{\Omega_R^2}. \tag{9}$$

When the condition $\tau_c \gg t_\pi$ does not hold (the noise does not change slow enough) we have to perform the double integral:

$$\left\langle\Delta\theta^2\right\rangle = \int_{-t_\pi/2}^{t_\pi/2} dt \int_{-t_\pi/2}^{t_\pi/2} dt' \left\langle\Delta\Omega(t)\Delta\Omega(t')\right\rangle \tag{10}$$

After a change of variables, $t' = t + \tau$, we recognize $R_\Omega(\tau) = \langle\Delta\Omega(t)\Delta\Omega(t+\tau)\rangle$ as the auto-correlation function of the noise. The auto-correlation $R(\tau)$ is related to $S(\omega)$, the noise power spectrum density, by a Fourier relation [25]:

$$R_\Omega(\tau) = \frac{1}{2\pi}\int_{-\infty}^{\infty} d\omega e^{i\omega\tau} S_\Omega(\omega) = \int_{-\infty}^{\infty} df e^{i2\pi f\tau} S_\Omega(f). \tag{11}$$

Combining Eq. (10) and Eq. (11) using a general pulse shape $w(t)$ (for a π pulse $\int_{-\infty}^{\infty} dt \left\langle\Omega_R\right\rangle w(t) = \frac{\pi}{2}$) with a Fourier transform $\mathbb{F}w(t) = W(\omega)$, we get for the RMS error

$$\left\langle\Delta\theta^2\right\rangle = \int_{-\infty}^{\infty} df \left|W(f)\right|^2 S_\Omega(f). \tag{12}$$

Assuming a "simple" window- i.e. a pulse that rises monotonously and then falls monotonously, the function $W(\omega)$ is centered about DC and therefore Eq. (12) represents filtering out of high frequency components of the noise. As an example, for the simple case of rectangular pulse of duration t_π:

$$\left\langle \Delta\theta^2 \right\rangle = t_\pi^2 \int_{-\infty}^{\infty} df \left(\frac{\sin(2\pi f \frac{t_\pi}{2})}{2\pi \frac{t_\pi}{2}} \right)^2 S_\Omega(\omega) = \frac{\pi^2}{4} \int_{-\infty}^{\infty} df \,\mathrm{sinc}^2(\pi f t_\pi) \frac{S_\Omega(f)}{\Omega_R^2} \tag{13}$$

Note that if we know the details of the power spectrum of the classical noises, and if significant power of the noise is concentrated in a narrow band of frequencies, then it is advantageous to design such a pulse $w(t)$ to reject the noise in these frequencies [26].

2.8.2 Spontaneous Scattering:

The other source of errors is quantum in nature and results in spontaneous scattering of photons. Only Raman scattering may induce errors since it changes the internal state of the ion and so we write $\hat{\rho}_{final} = (1 - P_{Raman}) \left|\psi_{ideal}\right\rangle \left\langle\psi_{ideal}\right| + \hat{\rho}_{error}$. Here $\hat{\rho}_{error} = \sum_i w_i \left|i\right\rangle \left\langle i\right|$ is the erroneous part of $\hat{\rho}_{final}$ with $P_{Raman} = \sum_i wi$, the probability for a Raman scattering event to occur. Some Raman scattering events may project the ion to a state which is not orthogonal to the ideal final state and therefore the term $\hat{\rho}_{error}$ may contain some positive contribution to the fidelity, which we neglect [18].

The total rate for the off-resonant scattering of photons from the Raman beams is given by the sum of probabilities P_i to occupy each intermediate state multiplied with it's decay rate γ_i [18, 19]:

$$\Gamma_{total} = \sum_i P_i \gamma_i = \sum_i \sum_{q=\{r,b\}} \sum_{m_s=\{\uparrow,\downarrow\}} \frac{P_{ms} \gamma_i \left|\left\langle m_s \left| \mathbf{d} \cdot E_q \hat{\varepsilon}_q \right| i \right\rangle\right|^2}{\Delta_i^2}. \tag{14}$$

With $\gamma_i = \gamma$ and $g_b = g_r = g$ and neglecting the qubit separation ω_m w.r.t. the detuning ($\omega_m \sim$ few MHz, $\Delta \sim$ few THz), we get

$$\begin{aligned}
\Gamma_{total} &= \gamma g^2 \left[P_\downarrow \left(\frac{\frac{1}{3}e_0^2 + \frac{2}{3}e_+^2}{\Delta^2} + \frac{\frac{2}{3}e_0^2 + \frac{1}{3}e_+^2}{(\Delta - \omega_f)^2} \right) + P_\uparrow \left(\frac{\frac{1}{3}e_0^2 + \frac{2}{3}e_-^2}{\Delta^2} + \frac{\frac{2}{3}e_0^2 + \frac{1}{3}e_-^2}{(\Delta - \omega_f)^2} \right) \right] = \\
&= \gamma \frac{g^2}{3} \left[\left(P_\downarrow + P_\uparrow\right) e_0^2 \left(\frac{1}{\Delta^2} + \frac{2}{(\Delta - \omega_f)^2} \right) + \left(P_\downarrow e_+^2 + P_\uparrow e_-^2\right) \left(\frac{2}{\Delta^2} + \frac{1}{(\Delta - \omega_f)^2} \right) \right] = \\
&= \gamma \frac{g^2}{3} \left[e_0^2 \left(\frac{1}{\Delta^2} + \frac{2}{(\Delta - \omega_f)^2} \right) + \frac{\left(e_+^2 + e_-^2\right)}{2} \left(\frac{2}{\Delta^2} + \frac{1}{(\Delta - \omega_f)^2} \right) \right],
\end{aligned} \tag{15}$$

where the last step assumes that $P_\uparrow = P_\downarrow = \frac{1}{2}$, a reasonable assumption during a π pulse from $|\downarrow\rangle$ to $|\uparrow\rangle$.

Another useful simplification is to take $e_0^2 = \frac{1}{2}$, $e_\pm^2 = 1/4$, e.g. a linearly polarized beam with a $\vec{k}$ vector perpendicular to the quantization axis and a polarization at 45 degrees to the quantization axis. This is the configuration used in the experiment. With that we get for the total scattering rate

$$\Gamma_{total} = \gamma \frac{g^2}{3} \left(\frac{1}{\Delta^2} + \frac{5/4}{(\Delta - \omega_f)^2} \right). \tag{16}$$

The total spontaneous scattering rate includes contributions from both Rayleigh and Raman scattering processes, but only Raman scattering causes errors and reduces the fidelity [18]. The rate for the different scattering processes is calculated from the Kramer-Heisenberg formula [27],

$$\Gamma_{i\to f}^{p} = \gamma g_p^2 \left| \frac{a_{i\to f}^{(p,J=1/2)}}{\Delta} + \frac{a_{i\to f}^{(p,J=3/2)}}{\Delta - \omega_f} \right|^2, \tag{17}$$

here $g_p = g \cdot e_p$ for $p = 0, +, -$ and $a_{i\to f}^{J} = \sum_q \sum_{e\in J} \frac{\langle f|\mathbf{d}\cdot\hat{\sigma}_q|e\rangle\langle e|\mathbf{d}\cdot\hat{\sigma}_k|i\rangle}{\mu^2}$, where $a_{i\to f}^{J}$ is a sum over pair products of appropriate Clebsch-Gordan coefficients (the matrix elements are normalized by the reduced matrix elements). Raman scattering events are inelastic with $i \neq f$. Rayleigh scattering events are elastic with $i = f$. The total rate for Raman scattering from $|\downarrow\rangle$ to $|\uparrow\rangle$ is given by the sum over polarizations: $\Gamma_{\downarrow\to\uparrow}^{tot} = \sum_k \Gamma_{\downarrow\to\uparrow}^{p}$. This is an in-coherent sum over p since in principle the scattered photon polarization and wavelength can be detected, but are averaged on. Writing the $|\downarrow\rangle \to |\uparrow\rangle$ Raman scattering rate explicitly we get

$$\Gamma_{\downarrow\to\uparrow}^{tot} = \gamma \left(g_0^2 \left| \frac{-\sqrt{\frac{2}{3}}\sqrt{\frac{1}{3}}}{\Delta} + \frac{\sqrt{\frac{1}{3}}\sqrt{\frac{2}{3}}}{\Delta - \omega_f} \right|^2 + g_+^2 \left| \frac{-\sqrt{\frac{1}{3}}\sqrt{\frac{2}{3}}}{\Delta} + \frac{\sqrt{\frac{2}{3}}\sqrt{\frac{1}{3}}}{\Delta - \omega_f} \right|^2 \right) =$$

$$= \frac{2}{9}\gamma(g_0^2 + g_+^2) \left| \frac{\omega_f}{\Delta(\Delta - \omega_f)} \right|^2.$$

We assume equal population in the $|\uparrow\rangle$ and $|\downarrow\rangle$ states and get for the total Raman scattering rate,

$$\Gamma_{Raman}^{tot} = \frac{1}{2}\Gamma_{\downarrow\to\uparrow}^{tot} + \frac{1}{2}\Gamma_{\uparrow\to\downarrow}^{tot} = \frac{1}{9}\gamma(2g_0^2 + g_+^2 + g_-^2) \left| \frac{\omega_f}{\Delta(\Delta - \omega_f)} \right|^2 =$$

$$= \frac{1}{9}\gamma g^2(2e_0^2 + e_+^2 + e_-^2) \left| \frac{\omega_f}{\Delta(\Delta - \omega_f)} \right|^2 = \frac{\gamma g^2}{6} \left| \frac{\omega_f}{\Delta(\Delta - \omega_f)} \right|^2, \tag{18}$$

where in the last step we assume $e_0^2 = \frac{1}{2}$, $e_\pm^2 = \frac{1}{4}$. The rate for Rayleigh scatterings is similarly calculated

to be

$$\Gamma^{tot}_{Rayleigh} = \frac{1}{2}\Gamma^{tot}_{\downarrow\to\downarrow} + \frac{1}{2}\Gamma^{tot}_{\uparrow\to\uparrow} =$$
$$= \frac{\gamma}{2}\left(2g_0^2\left|\frac{\sqrt{\frac{1}{3}}\sqrt{\frac{1}{3}}}{\Delta} + \frac{\sqrt{\frac{2}{3}}\sqrt{\frac{2}{3}}}{\Delta-\omega_f}\right|^2 + (g_+^2+g_-^2)\left|\frac{\sqrt{\frac{2}{3}}\sqrt{\frac{2}{3}}}{\Delta} + \frac{\sqrt{\frac{1}{3}}\sqrt{\frac{1}{3}}}{\Delta-\omega_f}\right|^2\right) =$$
$$= \frac{\gamma g^2}{2}\frac{1}{9}\left(2e_0^2\left|\frac{3\Delta-\omega_f}{\Delta(\Delta-\omega_f)}\right|^2 + (e_+^2+e_-^2)\left|\frac{3\Delta-2\omega_f}{\Delta(\Delta-\omega_f)}\right|^2\right) =$$
$$= \frac{\gamma g^2}{2}\frac{1}{9}\left(\left|\frac{3\Delta-\omega_f}{\Delta(\Delta-\omega_f)}\right|^2 + \frac{1}{2}\left|\frac{3\Delta-2\omega_f}{\Delta(\Delta-\omega_f)}\right|^2\right). \quad (19)$$

The sum of the Raman and Rayleigh scattering rates calculated from the Kramers-Heisenberg formula is of-course equal to the total scattering rate calculated earlier. The ratio of Raman to Rayleigh is

$$\frac{\Gamma_{Raman}}{\Gamma_{Rayleigh}} = \frac{2\omega_f^2}{9\Delta^2 + 3\omega_f^2 - 8\omega_f\Delta} \quad (20)$$

and for $\Delta \gg \omega_f$ reduces quadratically with Δ. We can also calculate the probability for a Raman scattering event during a π gate. For this we have $t_\pi = \frac{\pi}{2|\Omega_R|}$ and $P_{Raman} = t_\pi\Gamma_{Raman}$:

$$P_{Raman} = \varepsilon_s = \frac{\pi}{2}\frac{1}{2\sqrt{2}}\frac{1}{b_0 r_- + b_+ r_0}\frac{\gamma}{\Delta}\left|\frac{\omega_f}{\Delta-\omega_f}\right|. \quad (21)$$

P_{Raman} is the total probability to Raman scatter a photon during a σ_x gate. However - this is only an upper bound on the error since some Raman scattering events will return the qubit to the a state which isn't orthogonal to the state ideally obtained and these have some positive contribution to the fidelity. Some scattering events transferr the ion to the $4D_{\frac{5}{2}}$ or $4D_{\frac{3}{2}}$ levels. These events occur with a branching ration of $f \approx 1/14$ and results in complete loss of coherence, and therefore an error ε_D, where $\varepsilon_D = t_\pi f \Gamma^{\text{tot}}$.

3 Experimental System and Methods

3.1 Linear Paul Trap

The trap we built is similar to the configuration of figure 3, it is made of tungsten needles (0.3mm and 0.2mm in diameter) held by alumina wafers with adequate holes. The trap is assembled in an octagonal

shaped vacuum chamber with 6 available view-port windows for laser accessing and imaging. A pressure is below 8×10^{-12} Torr and is achieved by a combined use of an ion pump, a Titanium sublimation pump (TSP) and a non-evaporative getter pump. Strontium ions are created in the trap by photo-ionizing thermally evaporated neutral Strontium atoms. A neutral strontium source is realized by resistively heating a stainless steel tube containing solid strontium grains. A helical resonator (RF cavity) with $Q \approx 70$ is used in order to obtain the necessary high voltage (200 V at 20 MHz) on the trap electrodes. We have measured a secular harmonic frequency of $\omega_r/2\pi = 2\,\text{MHz}$ in the radial direction and up to $\omega_a/2\pi = 1\,\text{Mhz}$ in the axial direction.

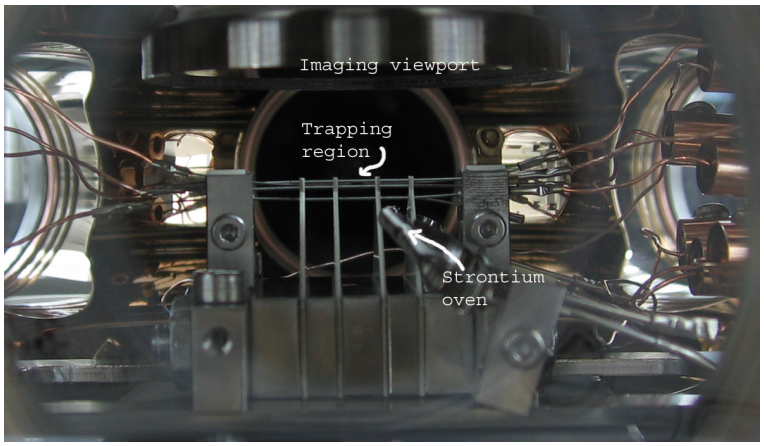

Figure 7: Ion trap.
Photo taken through one of the vacuum chamber view-ports. The trap electrodes are visible, together with a strontium oven and the imaging system view-port, which is into the vacuum chamber in order to maximize the solid angle of the objective.

3.2 Imaging System

All our planned experiments are based on the measurement of photons that are spontaneously scattered by the ions. The direction of fluorescence collection is perpendicular to the magnetic field that defines the quantization axis and the beams propagation direction. A 0.31 numerical aperture objective lens that corrects for the view-port spherical aberrations collects the fluorescence light from the ion. A flipping mirror switches between two possible measurements: either a diffraction limited imaging of the ions onto a CCD camera, or single photon counting by two photomultiplier tubes (PMT) each on a different side of a polarizing beam splitter (PBS) cube.

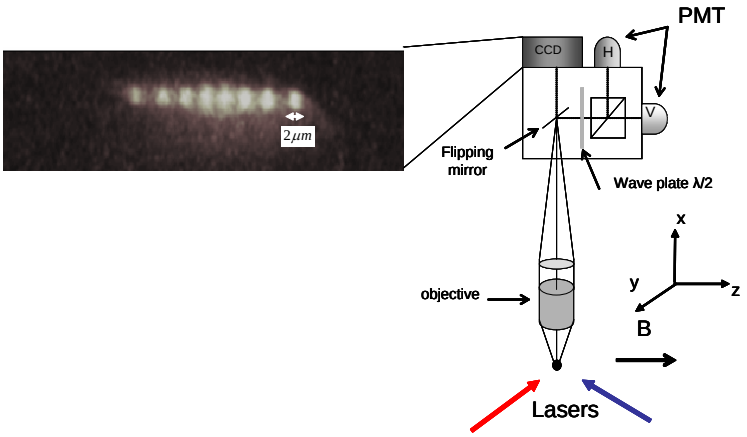

Figure 8: Imaging System.
Photons are collected by a large numerical aperture objective (N.A.=0.31) and are either polarization analyzed by a PBS and 2 counting PMTs or imaged on a EMCCD camera.

3.3 Lasers

Eight different lasers are needed to access all the relevant transitions of ^{88}Sr and $^{88}Sr^{+}$. They are listed by their wavelengths and function in table 2.

Table 2: Lasers - listed by wavelength

Wavelength	function
422 nm	Doppler cooling and fluorescence detection on $5S_{\frac{1}{2}} \rightarrow 5P_{\frac{1}{2}}$ transition
408 nm	Photon scattering on $5S_{\frac{1}{2}} \rightarrow 5P_{\frac{3}{2}}$ transition
461 nm	A doubled 922 nm ECDL made by Toptica. Used for photo-ionization
405 nm (free running)	Used for photo-ionization
405 nm (ECDL)	Raman transitions between the $5S_{\frac{1}{2}}$ qubit states
674 nm	Electron shelving from $5S_{\frac{1}{2}}$ to $4D_{\frac{5}{2}}$
1092 nm	Repumping from $4D_{\frac{3}{2}}$ to $5P_{\frac{1}{2}}$
1033 nm	Repumping from $4D_{\frac{5}{2}}$ to $5P_{\frac{3}{2}}$

ECDL All the lasers used in the experiment are diode lasers. In general, diode lasers are relatively low cost and offer good efficiency, stable operation, compact size and good noise characteristics. However, free-running laser diodes emit a broad frequency spectrum and are prone to longitudinal mode-hops. Even diodes that are sold as single mode diodes may exhibit mode-hopes with the slightest change of temperature or drive current. Also, tuning the laser to an exact atomic transition wavelength in a stable manner is impossible. Fortunately, stable single mode operation and tunability can be achieved by extending the diode laser internal cavity by additional frequency selective elements such as a diffraction

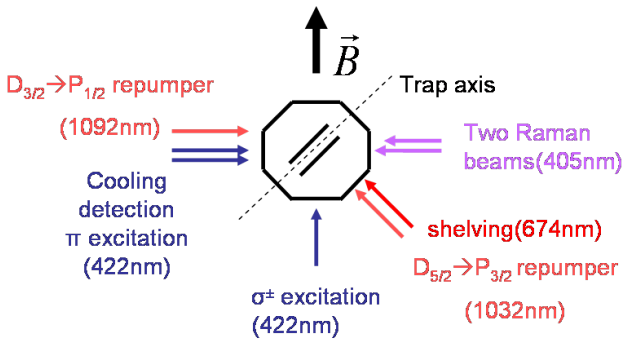

Figure 9: Schematic diagram of the experimental system.
Diagram shows magnetic field direction relative to laser propagation and polarization directions. Beam polarization is defined with respect to the quantizing magnetic field direction.

grating. A simplified schematic of this extended cavity laser is shown in figure 10a. The configuration shown is called the "Littrow" configuration. A diffraction grating is used to reflect the laser beam back into the laser diode and thus an extended cavity is closed between the grating and the back facet of the diode. The grating acts as a spectral filter and efficiently reflects only a narrow band of wavelengths. The spectral resolution of a diffraction grating is approximately given by $\frac{\Delta\lambda}{\lambda} \approx \frac{\lambda}{N_l}$ where N_l is the number of lines illuminated by the beam. The frequency band can be selected by adjusting the angle of the grating with respect to the laser beam. The free spectral range (FSR $= \frac{c}{2L}$, with L the length of the cavity and c the speed of light) of the extended cavity is much smaller than that of the laser diode since it is much longer than the internal cavity of the diode (typically $\approx$ few hundred μm). Ideally, as a result of mode competition only one of the external cavity modes that enjoys the most gain will be selected by the laser. The gain is a product of the internal mode structure, the gain profile, the grating wavelength selection function and the external modes (see figure 10b). It is possible to tune the frequency of the laser by rotating the grating (to change the maximally reflected wavelength) or by changing the length of the external cavity (to shift the modes of the cavity).

3.3.1 422 nm, Cooling and Detection

The 422 nm laser is a doubled diode laser manufactured by Toptica. The master laser is a 844 nm laser that is doubled using a non-linear crystal. The doubling is done with high efficiency ($\approx$ 10%) by placing the crystal in a cavity and locking the cavity to the laser by the method of Pound-Drever-Hall. The emission wavelength is locked to a Rubidium 87 line at 422 nm. By a lucky coincidence, the Rubidium line is only 440 MHz red of the $S_{\frac{1}{2}} \rightarrow P_{\frac{1}{2}}$ transition of $^{88}Sr^{+}$ used for Doppler cooling on the trapped ion and for fluorescence detection.

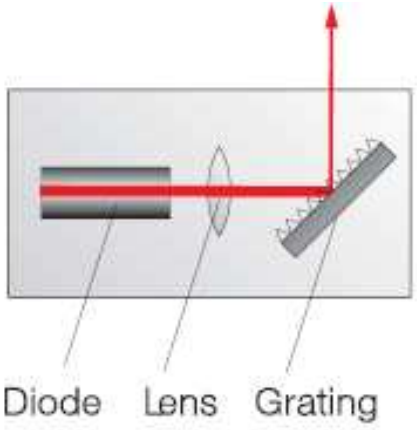

(a) Schematic of an ECDL in the Littrow configuration.

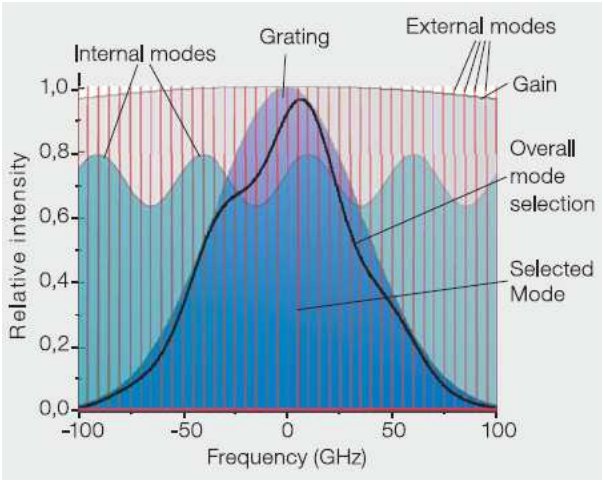

(b) Mode selection in ECDL.

Figure 10: Extended Cavity Diode Laser

graphics reprinted from http://www.toptica.com/products/itemlayer/32/BR-101-029-B-ProductCatalog-2008-04-SDL.pdf

(a) The output coupling of the laser is through the 0th order reflection from the grating, while the 1st order mode diffraction is used for frequency selective optical feedback. **(b)** As a result of mode competition only one of the external cavity modes that enjoys the most gain will be selected by the laser.

3.3.2 674 nm: Shelving

As mentioned in section 2.5 the detection scheme used must utilize a very narrow-band laser with line-width smaller than 1 kHz that is tuned to the $5S_{\frac{1}{2}} \leftrightarrow 4D_{\frac{5}{2}}$ transition. This is achieved by the method of locking the laser to a very high finesse and stable cavity. We use an ultra low expansion glass (ULE) cavity manufactured by ATF[3] and designed by JILA [28]. This special cavity has an expansion coefficient of $< 10^{-8}/^{\circ}C$, at room temperature and finesse of about 100,000. In order to take advantage of these qualities the cavity must be placed in a vacuum environment and isolated both thermally and acoustically.

3.3.3 1092 nm, 1033 nm: Re-pumps

These lasers are used to repump the ions from the D states as described in section 2.3.

3.3.4 405 nm,461 nm: Photo-ionization

The ionization of the neutral Strontium is done by two photon ionization. First a 461 nm laser (which is a doubled 921 nm DL) transfers the ion to $5s5p\,^1P_1$ level. Then a free-running 405 nm diode laser transfers it to the auto-ionizing level $5p^2\,^1D_2$. This method of ionization is more favorable than electron bombardment due to its larger cross-section and since only Sr is ionized, while electron bombardment

[3] http://www.atfilminc.com/

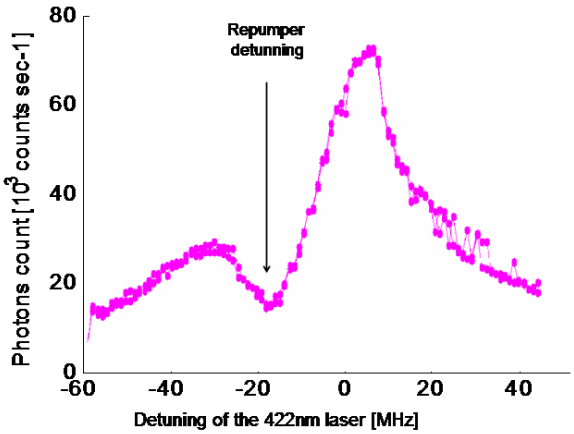

Figure 11: The $S_{\frac{1}{2}} \rightarrow P_{\frac{1}{2}}$ transition resonance as measured with the 422 nm laser.
The measurement shows fluorescence from the ion as the frequency of the 422 nm laser is scanned across the resonance. The minimum in the fluorescence is due to dark resonance with the repumper laser and it occurs at the repumper detuning. The flourecence spectrum is asymmetric with respect to positive and negative detuning: when red detuned the laser cools the ion while blue detuned laser heats it.

will ionize everything in their path, increasing the probability something other than Sr is trapped. This method also virtually eliminates charging of the trap electrodes and nearby structures that will cause stray electric fields and excess micro-motion [29].

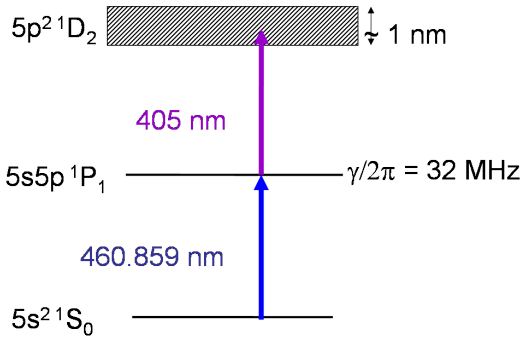

Figure 12: Photo-ionization- relevant levels of Sr

reprinted from Berkeland et-al, http://arxiv.org/PS_cache/quant-ph/pdf/0607/0607055v1.pdf

3.3.5 405.5 nm: Raman Transition

The design and construction of this laser is the focus of this thesis. The laser was built in-house from a violet Ga-Ni LD in the Littrow-ECDL configuration. The construction of this laser and the methods used to stabilize the Raman transition Rabi frequency are detailed in subsection 3.4.

3.4 Stabilized Raman Laser

The following section describes the construction of the laser, the methods used for passive stabilization of its output, the modulation of the laser that creates the sidebands needed for the Raman transition and the methods used for measuring and stabilizing the Rabi frequency of the Raman transition. The demands for stability follow from the desired fidelity. To achieve an error of 10^{-4} both the detuning and the intensity must be stabilized to 0.5%. While this level of stability is relatively easy to achieve for the detuning (0.5% of $\Delta - \omega_f$ is $\approx 22\,\mathrm{GHz}$), it is a challenge to stabilize the intensity to such a level. A schematic diagram of the laser system is given in figure 13.

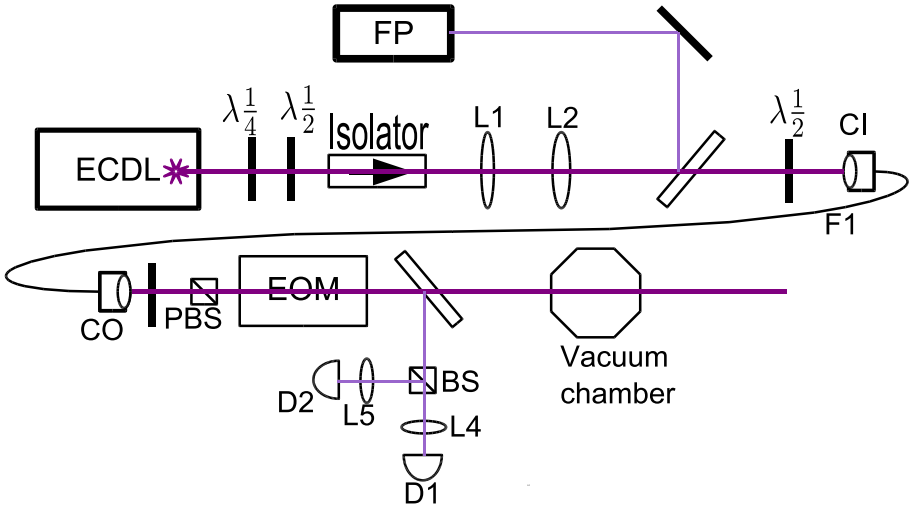

Figure 13: Raman-laser system, optical setup
The beam emerging from the ECDL is modematched by lenses L1 and L2 to the single mode optical fiber. Transmission efficiency through the fiber is close to 40%. The Fabre-Perot (FP) cavity is used to monitor the laser to verify that it is operating as single longitudinal mode. At the fiber output the laser is modulated by an EOM. The beam then enters the vacuum chamber. A pick-off window is used to sample the beam. The sample is measured by two photo detectors, D1 and D2, one is used for the servo control and the other is an independent sensor.

3.4.1 ECDL

The laser is an ECDL built in the Littrow configuration. The diode used is a blue-violet laser diode bought from Toptica. It is similar to laser diode used in blu-ray format optical storage devices. Figure 14 shows a photo of the laser.

The design is a standard one and almost identical to the one described in [30]. A few minor improvements on the basic design are:

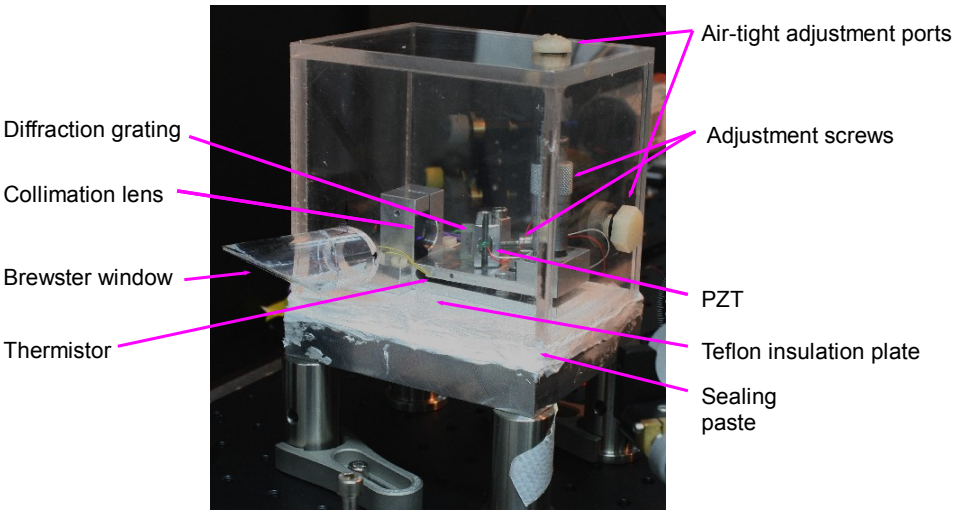

Figure 14: ECDL photo

1. The external cavity base-plate was insulated from the heat-sink by means of a Teflon plate. A thermo electric cooler (TEC) for temperature control of the base-plate and laser diode was attached to the heat-sink and the base-plate through a window in the Teflon insulation plate. The Teflon plate helps to prevent thermal fluctuations transferred from the heat-sink to the laser. The only heat conduction path is through the TEC, and is controlled by a servo circuit.

2. The entire apparatus was enclosed in an air-tight perspex box. Sealing the laser from the external atmosphere prevents fluctuations in the density of intra-cavity air causing fluctuations in the optical length of the external cavity - and hence frequency fluctuations. Before sealing the laser a jump of the laser frequency of about 10 MHz was observed each time the lab door was opened - see figure 15b (the lab is over-pressured with respect to the building). These jumps have completely disappeared once the laser was sealed.

3. The perspex box was covered with Polystyrene foam casing to further improve thermal insulation. The effect of insulation is apparent in sub-figure 15a where the wavelength of the laser during a removal and reinstalling of the casing was measured.

With the above modifications very good wavelength stability of the ECDL was obtained. Measurements made with a weak 5mW diode (not the diode finally used in the experiments) and strong (70%) optical feedback from a 2400 lines/mm holographic grating showed drifts smaller than 300MHz over a period longer than 22 hours as shown in figure 15c. For the final version of the laser a higher power LD with maximal output of 60 mW was used. Using strong optical feedback with this diode resulted the

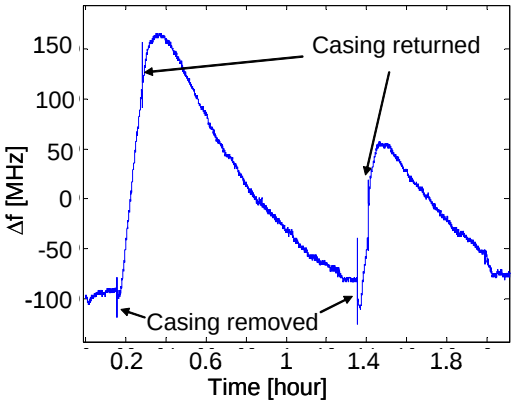

(a) Thermal effects.

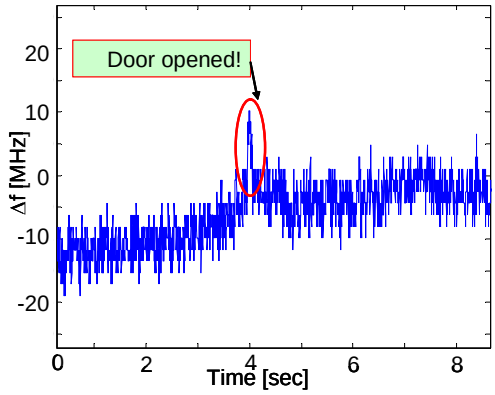

(b) Laser dependence on air pressure.

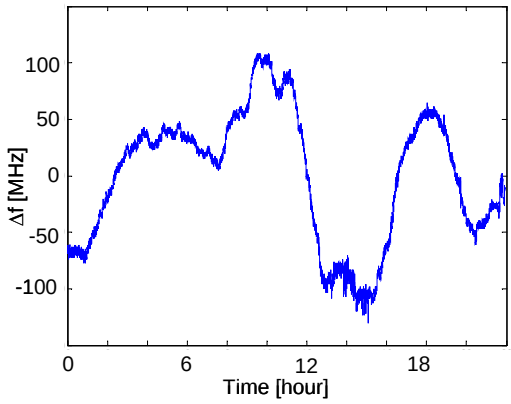

(c) Laser

Figure 15: Wavelength meter measurements, 5 mW ECDL, 70% optical feed-back
(a) Thermal insulation removed just before 0.2 hours and and replaced just after 0.2 hours. (b) Red circle shows where lab door was opened and then closed. (c) wavelength drifts over a 22hour period.

phenomenon of coherence collapse [31]: The laser, while tuneable with rotation of the grating, showed a very wide-band spectral feature (more than 1 GHz, the FSR of the Fabry-Perot cavity used in analysis). Moreover, interference fringes from the beam were of diminished visibility. As a solution a much weaker optical feedback was used in the final version of the laser. The grating used for the weak feedback on the high power laser is a holographic grating of 1200 lines/mm [Thorlabs part GH13-12V] and the *second* order of diffraction obeys the Littrow condition. Using the second order allowed for very weak optical feedback into the diode (feedback is ~4 %) while keeping frequency selectivity identical to a 2400 lines/mm grating. This relatively weak optical feedback degraded the stability of the laser, compared with the stability obtained with the low power strong feedback version used for the results in figure 15. However, there is no reason to believe that the improvements made to the stability by minimizing environmental effects on the laser do not contribute to the more powerful laser we now use.

3.4.2 Modulation, Creation of Sidebands

The laser is coupled to a polarization maintaining single mode optical fiber. At the output of the fiber the laser beam passes through an electro optical modulator (EOM) with the direction of polarization at 45 degrees to the axes of the EOM. The performance of an electro-optic modulator can be understood very simply as that of a retardation plate with electrically adjustable retardation[4]. In this configuration changes in the voltage applied to the EOM causes changes to the polarization of the output. The laser is modulated at about 3 MHz and sidebands at multiples of the modulation frequency are created to induce stimulated Raman transitions on the ion. To reach the relatively high voltage amplitude required ($V_{\lambda/2}$ of the EOM is close to 120 V) a simple serial LC circuit with $Q \approx 7$, FWHM of 400 kHz and resonant frequency of 3 MHz is used where the capacitance of 80 pF is entirely that of the EOM crystal and an inductor of 33 μH.

The initial (unmodulated) laser field is described by a classical electric field oscillating with angular frequency $\omega_0 = \frac{2\pi c}{\lambda_{laser}}$, $\vec{E}(t) = \vec{\varepsilon} E_0 \cos(\omega_0 t + kz + \phi)$, we choose $kz + \phi = 0$ at the ion. The beam is passed through an EOM with axes $\hat{x}, \hat{y}$. The axes are aligned such that $\hat{\varepsilon} = \frac{\hat{x}+\hat{y}}{\sqrt{2}}$. In the basis of the EOM axes we can write:

$$\vec{E}_{in}(t) = \frac{\hat{x}}{\sqrt{2}} E_0 \cos(\omega_0 t) + \frac{\hat{y}}{\sqrt{2}} E_0 \cos(\omega_0 t) \tag{22}$$

The field emerging from the modulator has a relative phase between the two polarizations, that depends on the applied voltage,

$$\vec{E}_{out}(t) = \frac{\hat{x}}{\sqrt{2}} E_0 \cos(\omega_0 t + \phi_x) + \frac{\hat{y}}{\sqrt{2}} E_0 \cos(\omega_0 t + \phi_y). \tag{23}$$

Assuming the $\hat{x}$ axis is parallel to the magnetic field applied at the position of the ion, $\vec{B} || \hat{x}$, we can write $\hat{x} = \hat{\pi}$ and $\hat{y} = i\frac{\hat{\sigma}_+ + \hat{\sigma}_-}{\sqrt{2}}$. The phase of each of the polarizations components $\hat{x}, \hat{y}$ is

$$\phi_{x,y} \quad = \quad \phi_{bx,y} + \phi_{dcx,y} + \beta_{x,y} \sin(\omega_m t + \phi_{rf}), \tag{24}$$

where ϕ_b is the phase retardation caused by the (thermally induced) static birefringence in the EOM, $\phi_{dc} = \pi \frac{V_{dc}}{V_{\lambda/2}}$ is phase induced by the DC component of the applied voltage and $\beta = \pi \frac{V_0}{V_{\lambda/2}}$. The applied RF voltage amplitude is V_0 and $V_{\lambda/2}$ is the half wave voltage for the EOM. The total applied voltage is $V(t) = V_{dc} + V_0 \sin(\omega_m t + \phi_{rf})$. The static birefringent phase can be added to the dc term in the voltage

[4] `http://www.linos.com/pages/home/shop-optik/elektro-optik/lasermodulatoren/technische-erlaeuterungen/`

induced birefringence so $\phi_b + \phi_{dc} \rightarrow \phi_b$. In these terms the field is

$$\vec{E}_{out}(t) = \frac{\hat{\pi}}{\sqrt{2}} E_0 \sum_{n=-\infty}^{\infty} J_n(\beta_x) \cos\left((\omega_0 + n\omega_m)t + \phi_{bx} + n\phi_{rf}\right) + \quad (25)$$

$$+ \quad i\frac{\hat{\sigma}_+ + \hat{\sigma}_-}{2} E_0 \sum_{n=-\infty}^{\infty} J_n(\beta_y) \cos\left((\omega_0 + n\omega_m)t + \phi_{by} + n\phi_{rf}\right), \quad (26)$$

where we use the following identity

$$\cos(\omega_0 t + \phi_b + \beta \sin(\omega_m t + \phi_{rf})) = Re\{e^{i\omega_0 t + i\phi_b + i\beta \sin(\omega_m t + \phi_{rf})}\} =$$

$$= Re\{e^{i\omega_0 t} e^{i\phi_b} \sum_{n=-\infty}^{\infty} J_n(\beta) e^{in(\omega_m t + \phi_{rf})}\} = \sum_{n=\infty}^{\infty} J_n(\beta) \cos((\omega_0 + n\omega_m)t + \phi_b + n\phi_{rf}). \quad (27)$$

We now calculate the Rabi frequency for stimulated Raman transitions, with the modulation scheme presented above. Using Eq. (6) and adding contributions from all the sidebands, we get:

$$\Omega_R = -ie^{i\phi_{rf}} \frac{\sqrt{2}}{3} g_b g_r \frac{\omega_f}{\Delta\left(\Delta - \omega_f\right)} \sum_{n=-\infty}^{\infty}$$

$$\frac{1}{2\sqrt{2}} \left[J_n(\beta_x) J_{n-1}(\beta_y) e^{i\left(\phi_{bx} - \phi_{by}\right)} + J_n(\beta_y) J_{n-1}(\beta_x) e^{i\left(\phi_{by} - \phi_{bx}\right)} \right]. \quad (28)$$

Using the Bessel function identities $J_n(x+y) = \sum_{k=-\infty}^{k=\infty} J_k(x) J_{n-k}(y)$ and $J_n(-x) = (-1)^n J_n(x)$, we get

$$J_n(x-y) = \sum_{k=-\infty}^{\infty} J_k(x) J_{k-n}(y). \quad (29)$$

Applying to the above $\sum_{n=-\infty}^{n=\infty} J_n(\beta_y) J_{n-1}(\beta_y) = J_1(\beta_x - \beta_y)$ we finally reach,

$$\Omega_R = \sin(\phi_{bx} - \phi_{by}) \frac{g_b g_r}{3} \frac{\omega_f}{\Delta\left(\Delta - \omega_f\right)} J_1(\beta_x - \beta_y) e^{i\phi_{rf}}. \quad (30)$$

β_x, β_y accounts for different modulation indices for the x,y axes. For the case where only the index of one of the axes is modulated we take $\beta \equiv \beta_x - \beta_y$ and

$$\Omega_R = \sin(\phi_{bx} - \phi_{by}) \frac{g_b g_r}{3} \frac{\omega_f}{\Delta\left(\Delta - \omega_f\right)} J_1(\beta) e^{i\phi_{rf}}. \quad (31)$$

With the Rabi frequency calculated here we get for the probability to scatter a Raman photon during a π

pulse (assuming we set $\Delta\phi_b = 0$ with proper choice of ϕ_{dc}):

$$P_{\text{Raman}} = \frac{\pi}{2}\frac{1}{2}\frac{1}{J_1(\beta)}\frac{\gamma}{\Delta}\left|\frac{\omega_f}{\Delta-\omega_f}\right|, \tag{32}$$

which depends on the fraction of light in the first order sidebands through the modulation index β.

symbol	parameter	calculated value
Ω_R	Rabi Frequency	$2\pi \times 13\,\text{kHz}$
t_π	π pulse time	$20\,\mu s$
Γ_{total}	Total scattering rate	$1.44\,\text{sec}^{-1}$
Γ_{Raman}	Raman scattering rate	$0.4\,\text{sec}^{-1}$
ε_s	Spontaneous scattering error	8×10^{-6}
$\frac{\Gamma_{Raman}}{\Gamma_{Rayleigh}}$	Raman to Rayleigh ratio	0.33

Table 3: Values of different rates calculated from theory.
Here we assume a Gaussian laser beam with a waist of 20_μm, a wavelength of 405.5 nm, a total power of 2 mW and $J_1(\beta) = \sqrt{2}J_1(\beta_{max})$.

3.4.3 Indirect Measurement of the Rabi Frequency

The Rabi frequency in Eq. (31) can be written in terms of the laser intensity I_0 , the static phase ϕ_b, the modulation index β and the detuning Δ,

$$\Omega_R = \frac{c^2}{\omega_0^3}\gamma\frac{\omega_f}{\Delta\left(\Delta-\omega_f\right)}\frac{\pi}{2\hbar}\sin(\phi_b)I_0 J_1(\beta)e^{i\phi_{rf}}. \tag{33}$$

Since we wish to keep the overall Rabi frequency stable, not just the intensity, a simple intensity noise-eater will not be enough on its own because it will not compensate for fluctuation in β and ϕ_b. However, if we are able to measure a signal proportional to the Rabi frequency continuously, a direct stabilization of the Rabi frequency is possible. This indeed can be done by the following method; We place a polarizer parallel to the incoming beam after the EOM. Using Eq. (23) the resulting field after the polarizer is,

$$\vec{E}_{PBS,||} = \left(\vec{E}_{out}\cdot\frac{\hat{x}+\hat{y}}{\sqrt{2}}\right)\frac{\hat{x}+\hat{y}}{\sqrt{2}} = \left[\frac{1}{\sqrt{2}}E_0\cos(\omega_0 t+\phi_x)+\frac{1}{\sqrt{2}}E_0\cos(\omega_0 t+\phi_y)\right]\frac{\hat{x}+\hat{y}}{\sqrt{2}}. \tag{34}$$

The intensity is proportional to $|E|^2$, averaged over $t > \frac{2\pi}{\omega_0}$,

$$\vec{E}_{PBS,||} \cdot \vec{E}_{PBS,||} = \frac{1}{2}E_0^2 \left[\cos^2(\omega_0 t + \phi_x) + \cos^2(\omega_0 t + \phi_y) + 2\cos(\omega_0 t + \phi_x)\cos(\omega_0 t + \phi_y)\right]$$

$$\Downarrow$$

$$I \sim \frac{1}{2}E_0^2 \left[1 + \cos(\phi_x + \phi_y)\right]. \tag{35}$$

With $\phi_{x,y}$ defined above we get that the intensity after a PBS,

$$I \sim \frac{1}{2}E_0^2 \left[1 + \cos(\phi_b + \phi_{dc}) \left(J_0(\beta) + 2\sum_{n=1}^{\infty} J_{2n}(\beta)\cos(2n(\omega_m t + \phi_{rf})) \right) \right.$$
$$\left. + 2\sin(\phi_b + \phi_{dc}) \sum_{n=0}^{\infty} J_{2n+1}(\beta)\sin((2n+1)(\omega_m t + \phi_{rf})) \right]. \tag{36}$$

The signal measured by a photo-detector is proportional to the intensity. This signal is multiplied (mixed) by a local oscillator $A\sin(\omega_m t + \phi_{LO})$ locked to the oscillator driving the EOM with relative ϕ_{LO} and and then low pass filtered. The filtered mixed down signal is proportional to the Rabi frequency,

$$V = K \times I_0 \sin(\phi_b + \phi_{dc}) J_1(\beta) \sin(\phi_{LO}), \tag{37}$$

with K including the quantum efficiency of the photo-detector, the trans-impedance gain and some conversion factor of the mixer.

3.4.4 Feedback

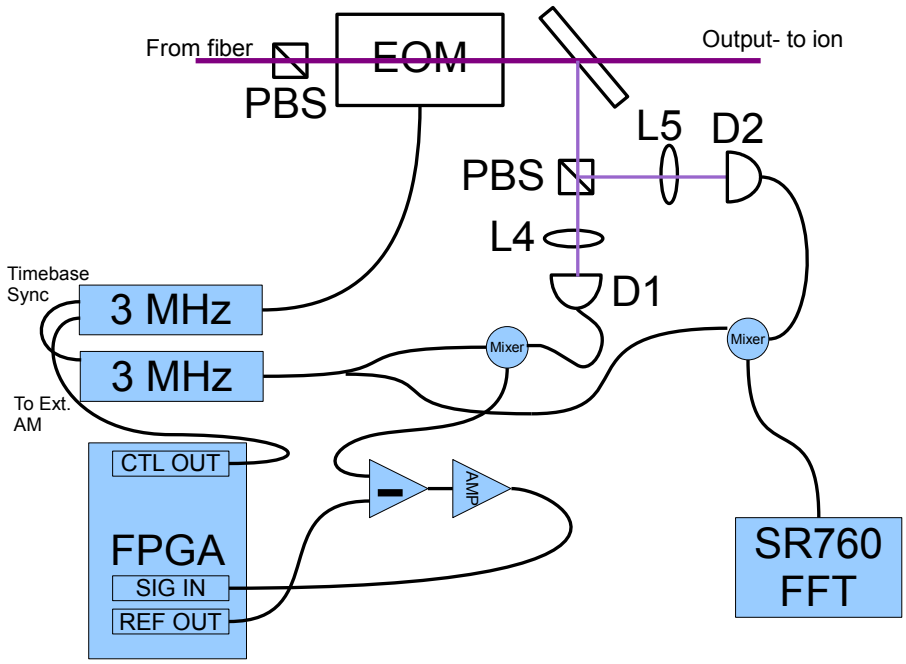

Figure 16: Raman laser - feedback scheme.
An EOM is modulating the beam to create sidebands. A pick-off window then samples the beam, before entering the vacuum chamber. The sampled beam is measured by D1, the servo system photo detector and D2, an independent detector. The voltage output of D1 is mixed down by a LO phase-locked to the modulation oscillator. An error signal is generated and passed to the FPGA card, which generate a control voltage passed to the external AM input of the modulating oscillator.

We aim to minimize the noise in the Rabi frequency Ω_R. The noise results from several factors. The main source is intensity noise caused by fluctuations of the coupling efficiency to the optical fiber. Other causes are thermally induced drifts of ϕ_b, the static birefringent phase of the EOM, and frequency drifts of the laser (to a smaller extent). The measured signal V contains also noises from the detection electronics and shot noise from the photo-detector. These extra noises that are not correlated to the noises of the "real" Rabi frequency seen by the ions, limits the best achievable performance of the system. Ideally, the only limiting factor should be the shot noise in the detected signal. For this case the system will be quantum noise limited. We show in figures 20 and 17 that the performance of our stabilization system is close to that fundamental limit. Measurements of the noise spectrum in V shows that all the power of the noise is concentrated in the low frequency band (few hundred Hz). At higher frequencies the noise flattens out. Measurements of the scaling of the noise power with the intensity of the signal revealed the spectraly flat noise at higher frequencies to be shot noise, together with some intensity independent noise (assumed to be electronic noise from the detector circuit). With these results the feedback system is designed to have

a significant gain in frequencies where the noise is acoustic and is correlated between the detector and the ion. The gain falls fast at higher frequencies so that the amount of noise that is injected into the laser beam is minimal [32].

The base-band (i.e. centered around DC) signal V is amplified and then subtracted from a reference voltage provided by the field programmable gate array (FPGA) card that is used for implementing the control system . The difference signal is then amplified once more and passes to the analog to digital converter (ADC) of the FPGA card. Passing the amplified error signal to the FPGA, instead of the raw measurement, improves the signal to digital quantization noise after the analog to digital conversion. Care was taken in order not to create ground loops and high impedance differential amplifiers were used for electrical separation of the signals to and from the FPGA and those originating at the optical setup. For more details refer to section 3.4.5. The signal was processed digitally and a control voltage is produced by the FPGA digital to analog converter (DAC) which is then applied as an input to the signal generator external amplitude modulation port, changing the amplitude of the RF signal modulating the laser beam. By constantly changing the amplitude of the modulation it is possible to counteract amplitude noises in the Rabi frequency. Formally, changing the amplitude of the modulating signal is equivalent to changing the modulation index β. Taking $\beta \to \beta_0 + \Delta\beta$, $\Omega_R \to \langle\Omega_R\rangle + \Delta\Omega_R$ to account for the control and the noise we have to first order in β

$$\Omega_R \sim I_0 \sin(\phi_{opt}) J_1(\beta_0) + I_0 \sin(\phi_{opt}) J_1'(\beta_0)\Delta\beta + \Delta\Omega_R = \\ = \langle\Omega_R\rangle \left(1 + \frac{J_1'(\beta_0)}{J_1(\beta_0)}\Delta\beta\right) + \Delta\Omega_R. \quad (38)$$

Ideally we would like $\Delta\beta = -\frac{\Delta\Omega_R}{\langle\Omega_R\rangle} \times \frac{J_1(\beta_0)}{J_1'(\beta_0)}$, then the noise would be canceled to first order. We assume that the noise is small enough in amplitude so that the control action $\Delta\beta$ is also small and contributions from higher orders of $J_1(\beta)$ are negligible. This also implies that it is desirable to choose β_0 such that the gain $\frac{J_1'(\beta_0)}{J_1(\beta_0)}$ and the normalized second derivative $\frac{J_1''(\beta_0)}{J_1(\beta_0)}$ is small. However, we would also like a high value of $\Omega_R \sim J_1(\beta_0)$. These two constraints are contradictory since working near the maximum of J_1 (to maximize the Rabi frequency) implies small values of its first derivative. We make the compromise of working close to 70% of the maximal value. In applying the control over the measured Rabi frequency rather than on the laser intensity alone we gain from two aspects. First, it is better conceptually to control a variable which is as similar as possible to the actual Rabi frequency. Since the Rabi frequency is a multiplication of several factors besides the intensity, fluctuations in those factors are not compensated

when stabilizing the intensity alone. A second reason is that in looking at a demodulated signal we are getting away from low frequency electrical noises in the electronics ("$1/f$ noises"). Thus we improve the signal to noise ratio in the measurement and consequently improve the feedback. This effect is apparent in figure 17 that shows measurement of the modulated-then-demodulated signal together with measurement of the intensity noises without the electro-optic modulator present in the beam path (referred in the figure as "noEOM"). Here RIN is relative intensity noise with respect to the shot-noise. The shot-noise level was measured by subtracting the electronic back-ground (measured with the beam blocked) from the signal and taking the asymptote as the shot noise.

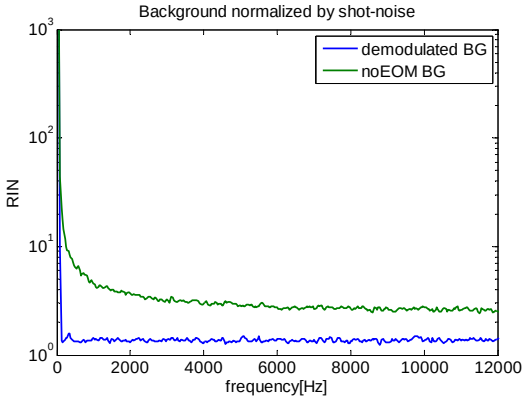

(a) Background noise density.

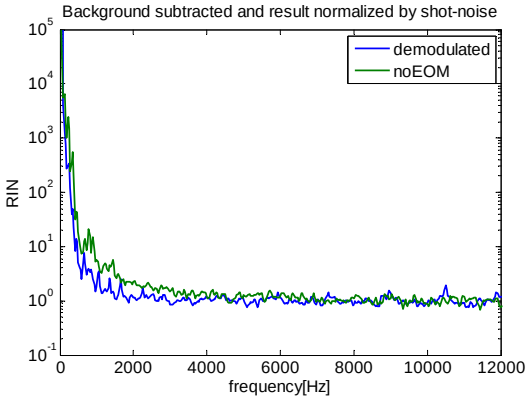

(b) Excess noise normalized to shot-noise.

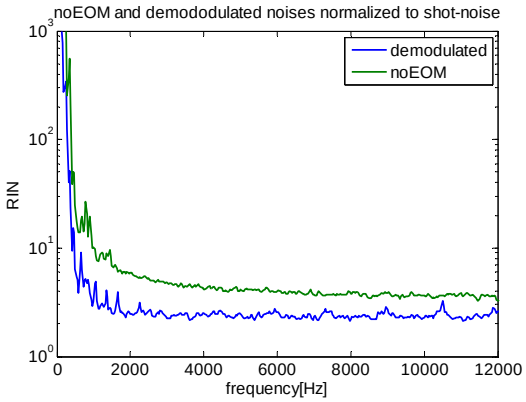

(c) Contribution from both excess and background noises.

Figure 17: Noise spectrum, both with and without demodulation
(a) Base-band measurement exhibits much greater background noise, compared with the demodulated signal. **(b)** Base-band measurement exhibits more excess noise. **(c)** Base-band shows stronger fluctuations over a greater bandwidth.

The most of the feedback loop is implemented digitally with a FPGA. We use a method outlined in [33] where the feedback is divided into two parallel paths, one responsible for maintaining a stable operation (very low frequency noise rejection) and the second is more wide-band, allowing for correction

of faster noise components. This is really just a P-I controller (Proportional - Integral), but with gain role-off also on the proportional signal path. This scheme worked well and allows for very stable operation (slow drifts are eliminated) and noise suppression up to about 2 kHz. The digital filters are simple, single pole infinite impulse response (IIR) systems, which are described by the difference equation (39), connecting the input at the discrete time-step n, $x[n]$ to the output $y[n]$,

$$y[n] = ay[n-1] + (1-a)x[n]. \tag{39}$$

Equation (39) is implemented in a straight-forward fashion in the FPGA (figure 18b). The frequency response is obtained by applying the z -transform $X(z) = \sum_{n=0}^{\infty} X[n]z^{-n}$, on the difference equation and evaluating it for $z = i\omega$[34]. We get

$$H(e^{i\omega}) = \frac{Y(e^{i\omega})}{X(e^{i\omega})} = \frac{1-a}{1-ae^{-i\omega}}, \tag{40}$$

where $\omega = 2\pi\frac{f}{f_s}$ is the discrete frequency. Approximating $H(i\omega)$ for frequencies $f \ll f_s$ we get $H(i\omega) \approx \frac{1-a}{1-a(1-i\omega)} = \frac{1}{1+i\frac{\omega}{1-a}}$, the frequency response of an analog single-poled low-pass filter, with corner frequency $\omega_c = 1-a$. A screen-shot of the control system Labview program is in figure 18a.

3.4.5 Electronics

In order to fully take advantage of the FPGA capabilities, some signal conditioning is needed prior to the A/D sampling done by the FPGA card. The ADC used has 16 bits of resolution and full scale of 20 volts. This implies a voltage resolution of 0.3 mV. With the active feedback the noise remaining in the signal cannot be controlled to better than 0.3 mV in amplitude, even under ideal conditions. We can effectively lower this limit by amplifying the signal before A/D conversion, but with a demodulated signal of approximately 500 mV the best we can do is a gain factor of 20. But, if the error signal is generated before the analog to digital conversion then the feedback will have the effect of bringing it to a mean value of 0 V. It is then possible to amplify the signal so that the noise will be measured with greater resolution. This is done by generating a reference voltage in the FPGA using it's DAC (digital to analog converter) and using an analog circuit for the subtraction. The resulting signal is then amplified by a factor of approximately 80. This procedure improved the resolution of the measurement to about $4\,\mu V$.

Another problem encountered is ground loops caused by the fact that the computer hosting the FPGA is placed fairly far away from the optical setup. This in turn results 50 Hz (and multiples) noise on the

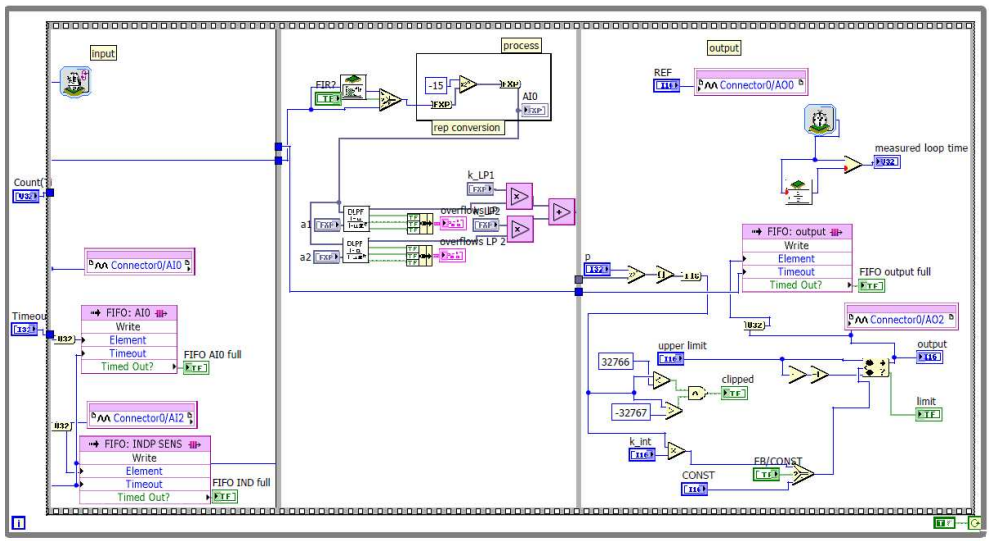

(a) FPGA target VI

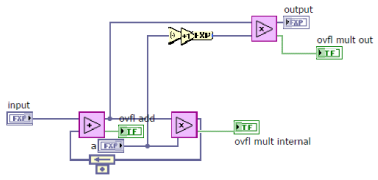

(b) Digital filter

Figure 18: Labview VI programs- digital implementation of control

signals. This problem was largely solved by introducing a high impedance differential amplifier on the reference signal produced by the FPGA. Moreover, the long cables were vulnerable to RF noises picked up from a noisy environment (AOM and EOM driven by amplified RF sources, the RF feeding the ion trap, etc.). These noises alone should not present a problem (since they are way outside the bandwidth of interest) but they can cause some dc bias in the electronics due to rectification[5]. Introduction of simple passive differential and common mode filters at the input of the amplifier took care of most of this effect. Implementing the control digitally requires sampling the signal. To avoid aliasing of high frequency noises to the low frequency base-band, an anti-aliasing filter is placed at the output of the amplifier, before the ADC.

The open loop (FPGA output to FPGA input through modulator and detector) transfer function is dominated by a single pole at 25 kHz. The pole is at a frequency much higher than the dominant components of noise we are trying to eliminate, so it does not affect the performance of the servo system. This single pole behavior is caused by the frequency response of the external AM input of the signal generator.

[5] http://www.analog.com/library/analogDialogue/Anniversary/14.html

4 Results

4.1 Performance of the Rabi frequency Servo Control System

4.1.1 Noise Characteristics

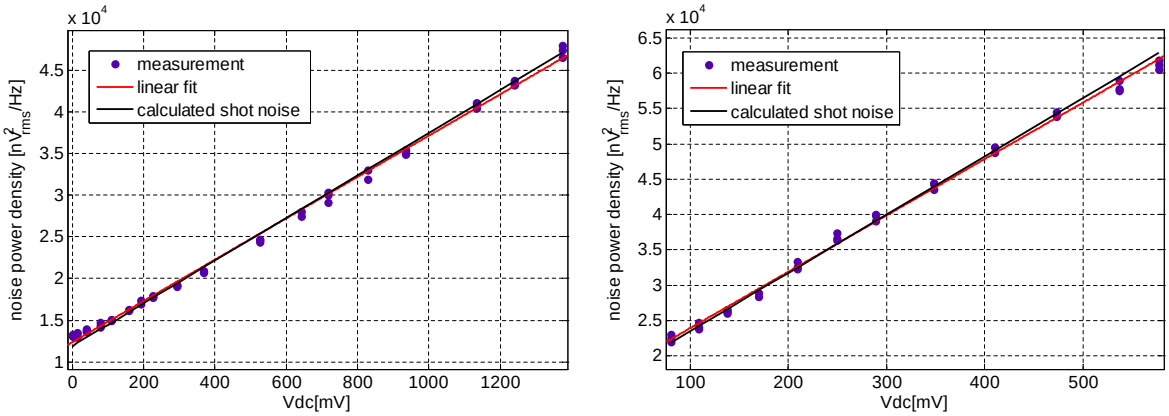

(a) V_{noise} vs. V_{dc} for intensity signal (no modulation or demodulation)

(b) V_{noise} vs. V_{dc} for demodulated signal

Figure 19: Dependence of noise floor on detected beam power.
Noise density is linear with beam intensity - signature of shot noise. Moreover, the fitted linear slope matches the calculation for shot noise density.

The noise consists mostly of very low frequency fluctuations where most of the energy of the noise is contained below 1 Hz. At higher frequencies the noise is dominated by the noise floor of the detector and the photo-current shot-noise, which are both white in the BW concerned. Figure 19 shows measurement of the noise density in a band dominated by white noises plotted against beam power measured by the same photo detector. The measurements are fitted to a linear function and the slope was compared with that expected from shot-noise. The expected shot noise noise density is calculated from the shot noise formula [35]. $V_{\text{sn,rms}} = \sqrt{2Be\overline{I_{dc}}}G_{\text{trans-imp}} = \sqrt{2Be\overline{V_{dc}}G_{\text{trans-imp}}}$ where B is the bandwidth of the measurement, e is the electron charge, $\overline{I_{dc}}$ is the photo current at the photo diode (proportional to the beam intensity) and $G_{\text{trans-imp}}$ is the trans-impedance gain of the amplifier following the photo diode. For the shot noise power density we get

$$P_{\text{sn}} = \frac{V_{\text{sn,rms}}^2}{B} = 2eG_{\text{trans-imp}}\overline{V_{dc}} \tag{41}$$

This relation is true for the noise density in an unmodulated beam but also for the noise in the modulated-then-demodulated signal, provided that $G_{\text{trans-imp}}$ is calibrated to include voltage conversion factors from

the mixer, as is justified in the appendix A.2. From the measured noise density it is apparent that it is linear with the beam intensity. Moreover, the proportionality constant extracted from the fitted linear slope, ($24.8 \pm 0.4\,\mathrm{nV_{rms}Hz^{-1}}$ for unmodulated beam and $80.0 \pm 1.6\,\mathrm{nV_{rms}Hz^{-1}}$ for the modulated-then-demodulated beam), is in good agreement with what expected from Eq. 41 ($25.6\,\mathrm{nV_{rms}Hz^{-1}}$ and $82.6\,\mathrm{nV_{rms}Hz^{-1}}$ accordingly). The small discrepancies are attributed to the poor signal to noise in the measurement (shot noise is of the order of detector electronic noise) and to the nonlinearities in the detection electronics. The performance of the Rabi frequency stabilization system was characterized using the experimental setup depicted in figure 16. The modulated laser beam was measured using two fast photo-detectors (Newfocus 125 MHz Si photo-detector 1801-FS), one used in the feedback loop ("in-loop" detector) that provides the signal for the feedback system and a second independent detector used to assess the performance of the feedback system. The signal from both detectors is mixed down and low pass filtered. The spectrum of both signals is measured using a FFT spectrum analyzer (SR760). Some measurements are given in figure 20.

4.1.2 Performance of the Feedback Loop

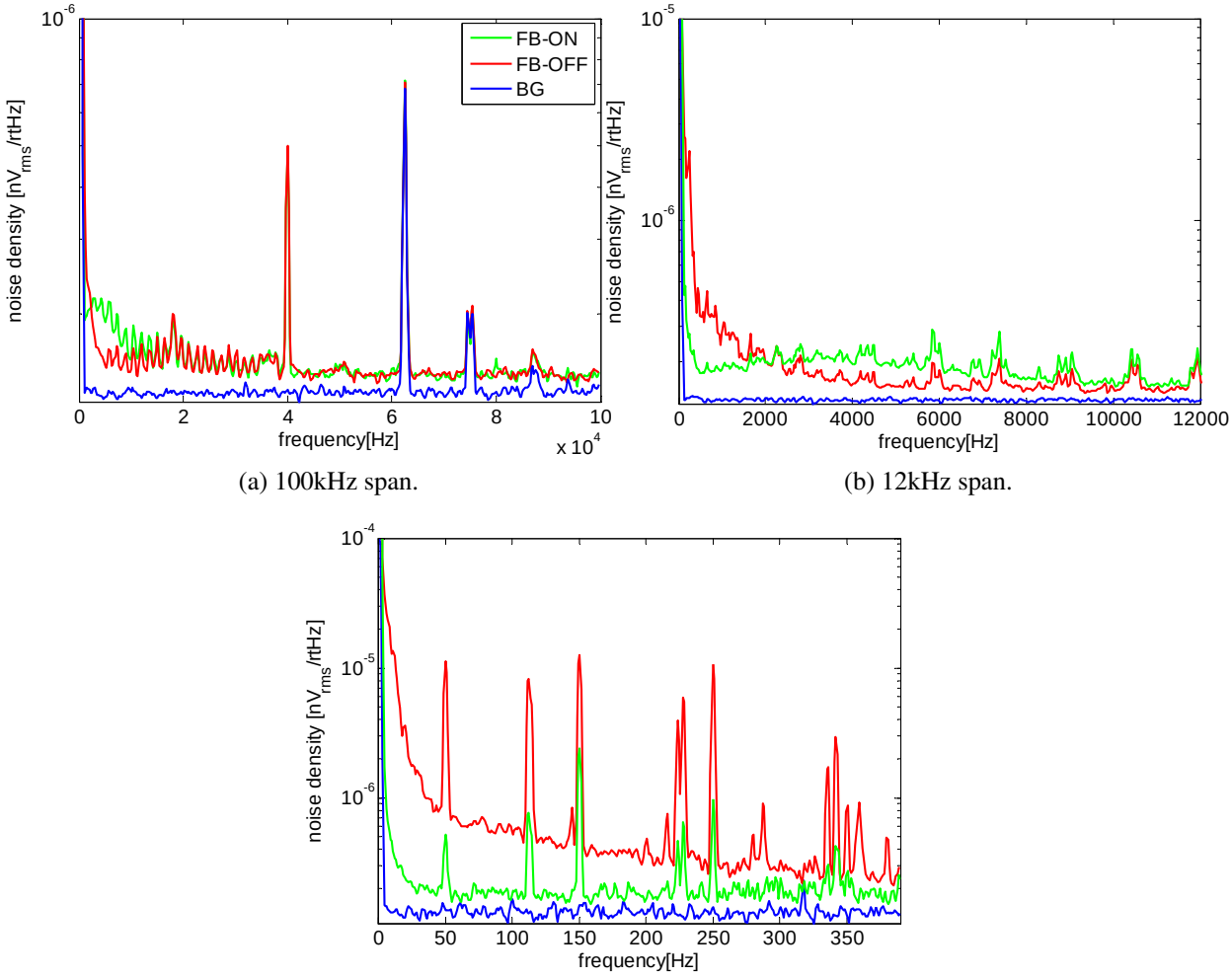

(a) 100kHz span.

(b) 12kHz span.

(c) 390Hz span.

Figure 20: Noise spectra for different span widths, independent sensor
BG: Back ground measurement where light is blocked. FB-ON,FB-OFF: feedback system is operating or idle, y axis in log scale. **(a)** The feedback system has no effect for frequencies $> 10\,\text{kHz}$. **(b)** There is some injected noise between 2 kHz and 10 kHz due to feedback gain being lager than unity. **(c)** Clearly show suppression of the noise in this frequency band.

The three sub-figures of figure 20 show the noise spectral density, as measured on FFT spectrum analyzer for different resolutions. The blue curves shows the measurement with the light blocked. The red and green lines shows the noise with the feedback system operating and idle, respectively. The noises at high frequencies are white (independent of frequency) and are measured to be the sum of the photo-current shot-noise together with the electronic noise floor of the detector (details in subsection 4.1.1). The spectral features at 62 kHz and 75 kHz are of unknown origin but since they exist even when the photo detector is blocked are most probably due to electronic pick up and have nothing to do with the

ion. The action of the feedback system is evident on the plots for frequency spans of 390 Hz and 12 kHz. A significant attenuation of the noise is achieved for frequencies below 2kHz. Between 2kHz and 10kHz the feedback is creating excess noise. In this range of frequencies, the noise is uncorrelated between the in-loop detector and the independent detector used for this measurement, but there is still significant gain of the feedback system so electrical noises from the detection circuit are injected into the system. Ideally the gain should have been much smaller in this region but this is technically very difficult to achieve. Above 12kHz there is no effect of the feedback (FB). For a more quantitative measurement of the effect of the FB we estimate the classical error accumulated over frequency using Eq.(12). The noise energy density up to a certain BW is integrated and then the noise from a reference high frequency band is subtracted: $\varepsilon_{c,measured} = \frac{1}{V_{dc}^2}\left[Var(LPF_{BW}\{V\}) - \frac{BW}{refBW} \times Var(BPF_{refBW}\{V\})\right]$. The result is the energy of the noise from classical fluctuations in the beam only. The electronic noises from the detector are not seen by the ion and the shot-noise is already accounted for by the spontaneous scattering error. We have succeeded in reducing the classical noises in the beam (not including beam pointing noises on the ion, which are out of the scope of this work) to a level lower than the errors expected from spontaneous scattering of photons.

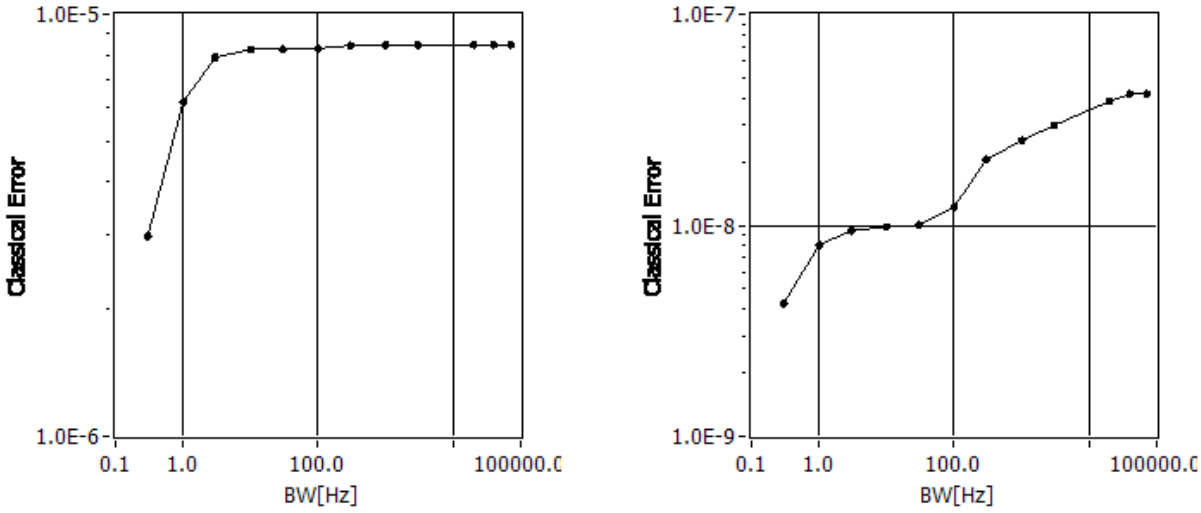

(a) Feed back OFF

(b) Feed back ON

Figure 21: Classical Errors as function of BW (log-log scale)
(a) Feedback off: classical errors in the presence of active stabilization reaching an asymptote of 8×10^{-6} for BW greater than 50 kHz. **(b)** Feedback on: classical errors reaching a level of 1×10^{-8} for BW exceeding few Hertz and leveling off at 4×10^{-8} for BW greater than 100 Hz. In both cases most of the noise energy is contained below 1 Hz. The feedback attenuated the overall error by a factor of ~270.

4.2 Measurement of the Spontaneous Scattering Rate

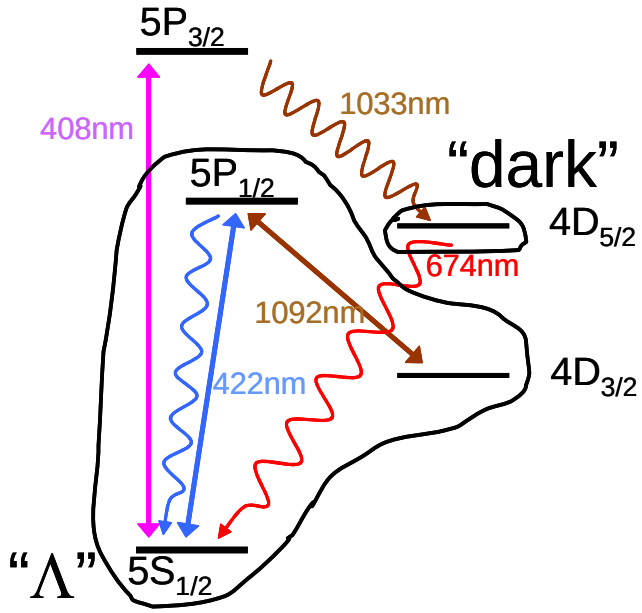

Figure 22: Definition of the "Λ" and "dark" states.
The Λ state is the subspace containing $5S_{\frac{1}{2}}, 5P_{\frac{1}{2}}$ and $4D_{\frac{3}{2}}$. The dark, or non-fluorescing state is the metastable $4D_{\frac{3}{2}}$.

We are able to estimate the actual spontaneous scattering rate, by measuring the rate the ion decays into the metastable state $4D_{\frac{5}{2}}$. The three levels $5S_{\frac{1}{2}}, 5P_{\frac{1}{2}}$ and $4D_{\frac{3}{2}}$ form a Λ configuration. As long as only the 422 nm and 1092 nm lasers are operating the ion will continuously fluoresce at a rate determined by the steady state population of the $P_{\frac{1}{2}}$. When 408 nm radiation is present, there is some population buildup in the $P_{\frac{3}{2}}$ state, outside the Λ configuration. This population can spontaneously decay either to the $S_{\frac{1}{2}}$ state (and return to the Λ) or to the $D_{\frac{5}{2}}$ state (with a branching ratio of $1/14$ [18]). If the ion decays to the $D_{\frac{5}{2}}$ fluorescence from the 422 nm laser stops, until the metastable $4D_{\frac{5}{2}}$ state decays with $\tau \approx 0.4$ S back into the Λ configuration. These quantum jumps can be detected and the rate at which they occur is measured. This rate, when multiplied by the branching ratio will provide an estimate of the total spontaneous scattering rate. When we attempt to perform this measurement, we find a scattering rate 2 orders of magnitude higher than expected from off resonance scattering by the 405.5 nm laser beam alone. This led to the conclusion that light resonant with the 408 nm $5P_{\frac{1}{2}} \rightarrow 5P_{\frac{3}{2}}$ transition is present in the beam. Indeed, after the placing a diffraction grating of 2400 lines/mm to spectraly filter the laser beam before the optical fiber leading to the ion-trap, the measured rate of the dark periods dropped significantly to a level close to what predicted by calculation, see details in subsection 4.2.1. The 408 nm light present

in the Raman laser is used to measure the lifetime of the $4D_{\frac{5}{2}}$ metasable state. We also use the high rate of dark events to better align the laser to illuminate the ion (by maximizing the quantum jump rate) and to measure the beam width at the ion position (the laser is far from saturating the transition).

4.2.1 Spontaneous Scatterings due to Off-resonant Light

As mentioned, a grating is used to filter out light resonant with the $5P_{\frac{1}{2}} \rightarrow 5P_{\frac{3}{2}}$ transition. A single ion is trapped and investigated. The experimental pulse sequence is 8 ms long and is repeated continuously for 1 hour (450,000 measurements). The pulse sequence was structured as follows:

1. 2 ms cooling pulse (using off-resonant 422 nm light)

2. 4 ms Raman laser pulse.

3. The sequence ends with a 2 ms detection pulse where photons scattered from 422 nm resonant light are counted by a PMT.

If the ion was transferred into the metastable state during the Raman pulse, it will not fluoresce during the subsequent detection pulse and the PMT counted photons at the background level, averaged at about 10 counts/2ms. If on the other hand the ion was not transferred to the metastable state, then it fluoresces during the detection pulse and an average of 60 photons/2ms are detected. The low scattering rate resulted 27 quantum jumps. This did not allow for any elaborate statistical analysis. However, the mean time between quantum jumps can be taken as an estimate of the time between scattering events (assuming constant probability for scattering per unit time). This resulted $T_{\text{scatter}} = 65 \pm 12\,\text{sec}$ or $R_{\text{scatter}} = 1/T = 0.0154 \pm 0.0030\,\text{sec}^{-1}$. The rate calculated from measured laser power (960 μW), beam width at the ion ($\approx 40\mu\text{m}$) and atomic parameters place this rate at $0.012\,\text{sec}^{-1}$, consistent with our measurement. Repeating the calculation for beam width $w = 37\,\mu\text{m}$ the exact measured quantum jump rate is obtained. This is reasonable when taking into account that the beam width was not measured with high accuracy. These results reassure that including the filtering diffraction grating in the setup indeed attenuates the on-resonance 408 nm radiation to undetectable level and that this will not be a limiting factor in future experiment. The expected error due to Raman photon scattering is thus verified to be that given in the table 3.

4.2.2 Measurements of the Lifetime of the $4D_{\frac{5}{2}}$ Metastable State

We use the same system, this time with the grating set to select only the 408 nm light from the laser. We get a high rate of quantum jumps events, enabling us to accumulate enough data to measure the lifetime of the $4D_{\frac{5}{2}}$ metastable state with good statistical accuracy. We also demonstrate photon antibunching of the 674 nm radiation field by looking at the statistics of the recovery time of the ion from the dark state. A single ion was trapped for this experiment. The experimental pulse sequence was 8 ms long and was repeated continuously for 1 hour (600,000 measurements). This time the 408 nm pulse was concurrent with a cooling pulse. The pulse sequence is:

1. 4 ms cooling pulse (using off-resonant 422 nm light) + 408 nm light
2. 2 ms detection pulse where photons scattered from the 422 nm resonant light are counted by a PMT.

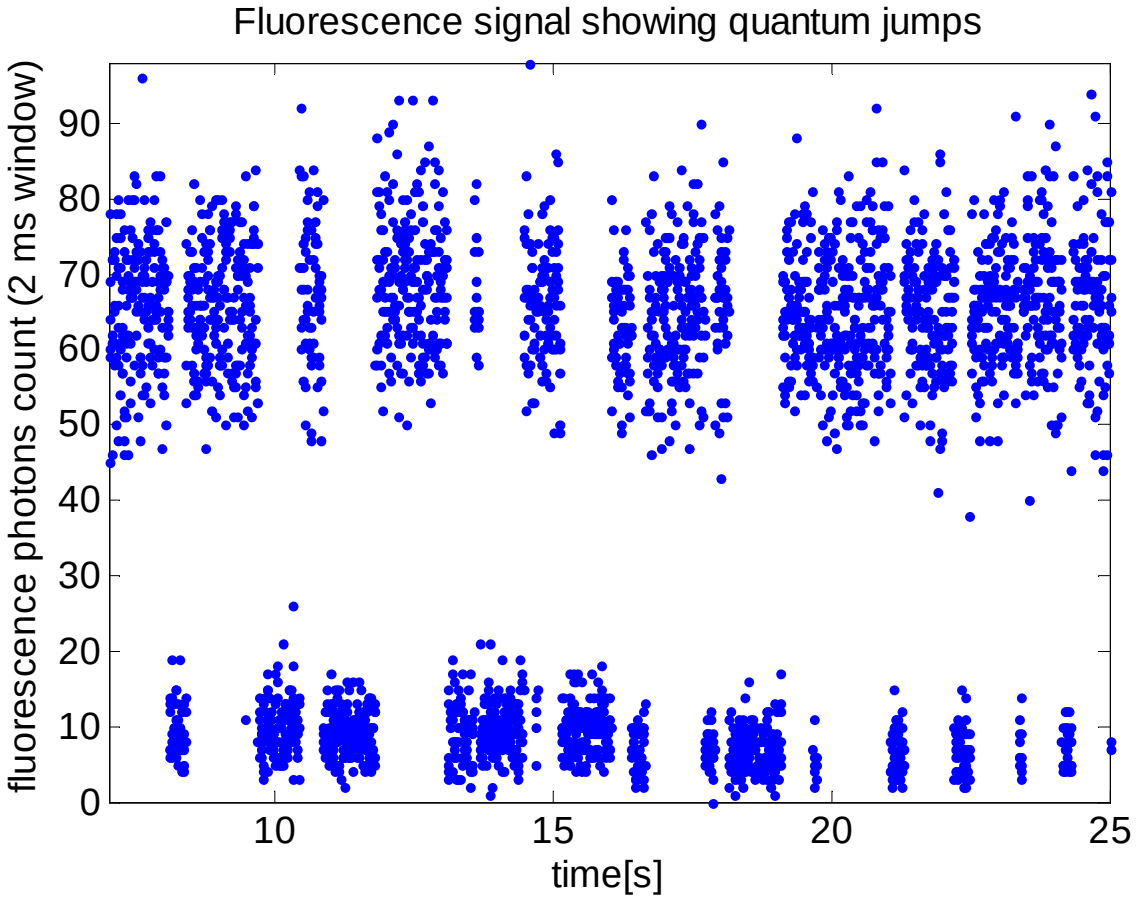

Figure 23: Observed fluorescence signal.
Quantum jumps to the $D_{\frac{5}{2}}$ level are indicated by the sudden reduction of fluorescence to background levels.

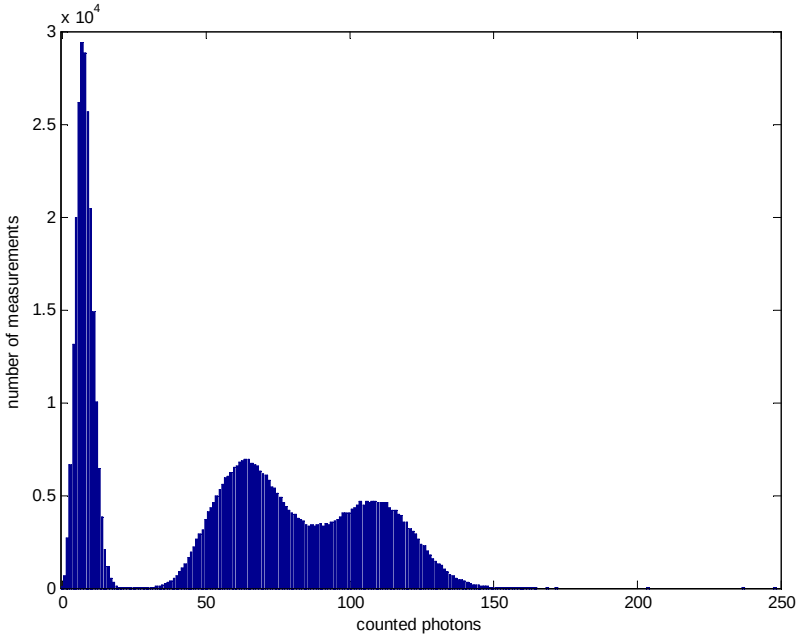

Figure 24: Histogram of number of photon counted in 2 ms
The left-most peak is due to background counts in the absence of an fluorescence. The middle and right peak are due to fluorescence. The wavelength of the 1092 nm repump changed during the measurements, resulting 2 distinct peaks. The 2 fluorescence peaks are well separated from the dark counts peak. A threshold is set at the minimum of the histogram, at 24 counts so any bin with less than 24 detected photons is considered dark and any bin with more than that number is considered bright.

After setting a threshold between dark and bright events the times at which quantum jumps (at which the ion goes dark) and decays of the metastable $4D_{\frac{5}{2}}$ (ion goes bright) occur are recorded. The duration of the each dark period is recorded and binned by the number of time samples it lasted, where each time sample is at the length of a single pulse sequence, 6 ms. We end up with 3117 dark events of different durations. The method of extended maximum likelihood is used to extract the lifetime from the data. Assuming exponential decay, the probability per unit time of an ion in the dark state to decay to the Λ configuration and continue to fluoresce is $p(t,\tau) = \frac{1}{\tau}e^{-t/\tau}$. Here τ is the lifetime of the $4D_{\frac{5}{2}}$ state. The probability of a measuring a dark duration that belongs in the i'th bin (the dark time durations are naturally binned by the number of time samples they lasted. this is a result of the finite time resolution of the measurement) is given by $P_i = \frac{1}{\tau}\int_{(i-1)t_s}^{it_s} dte^{-t/tau} = 2\sinh(\frac{t_s}{2\tau})e^{-t_i/\tau} \approx \frac{t_s}{\tau}e^{-t_i/\tau}$. Here t_s is the sample time (same as bin) duration assumed much smaller than the lifetime $\tau \gg t_s$ and t_i is the time assigned to the i'th bin $t_i = (i-\frac{1}{2})t_s$. Although the every dark period observed in the experiment was also observed to decay, it is beneficial to include a finite acceptance window T in the analysis. Defining a window of M samples we have $T = Mt_s$. The probability for a decay to be registered outside the acceptance window

is $P_{M+1} = \frac{1}{\tau}\int_{Mt_s}^{\infty} dt e^{-t/\tau} = e^{-Mt_s/\tau}$. In a of measurement where a single object undergoes a series of creations and decays (in contrast with estimation of lifetimes from a macroscopic sample) and where all the decays are accounted for, the number of decaying "particles", N_0 is known exactly. The likelihood function is the probability to have n_1 events in the first bin, n_2 events in the second bin, ... , n_{M+1} events in the last bin, and is given by the multinomial distribution:

$$L = P_{\{n_i\}} = \left(\begin{array}{c} N_0 \\ n_1,..,n_i,..,n_{M+1} \end{array} \right) P_1^{n_1} P_2^{n_2} \cdots P_{M+1}^{n_{M+1}} = (2\sinh(\frac{t_b}{2\tau}))^{\sum_{i=1}^{M} n_i} \times e^{-\frac{1}{\tau}\sum_{i=1}^{M} n_i t_i} e^{-Mt_b n_{M+1}/\tau}. \quad (42)$$

The sum $\sum_{i=1}^{M} n_i = N$ is just the number of events in the acceptance window, while $\sum_{i=1}^{M} n_i t_i = N\bar{t}$ where $\bar{t}$ is just the mean time of events in the acceptance window. With this definition, the numbers of events outside the acceptance window is $N_{M+1} = N_0 - N$. For convenience the log-likelihood is maximized instead of the likelihood:

$$\ln(L) = (\text{terms that do not contain } \tau) + N\ln(2\sinh(\frac{t_b}{2\tau})) - \frac{N\bar{t}}{\tau} - \frac{Mt_b}{\tau}(N_0 - N). \quad (43)$$

Demanding that the derivative with respect to τ vanishes to find the lifetime that maximizes the probability for a measurement:

$$\frac{\partial \ln L}{\partial \tau} = -\frac{t_b}{2\tau^2}\frac{1}{\tanh(\frac{t_b}{2\tau})} + \frac{\bar{t}}{\tau^2} + \frac{Mt_b(\frac{N_0}{N} - 1)}{\tau^2} = 0. \quad (44)$$

Approximating $\frac{x}{\tanh(x)} \approx 1 + \frac{1}{3}x^2$ ($x = \frac{t_b}{2\tau}$) and noting that with the known values for t_b, τ: $x \approx 2 \cdot 10^{-5}$ (this is justified since the error on the estimator far exceeds this number) we can take for the estimator the following expression:

$$\hat{\tau} = \bar{t} + Mt_b(\frac{N_0}{N} - 1). \quad (45)$$

This estimator for $\hat{\tau}$ is unbiased assuming that $\frac{1}{\langle N \rangle} \approx \left\langle \frac{1}{N} \right\rangle$ (which is a good approximation for $N \gg 1$). The error in this estimator for τ is,

$$\Delta\hat{\tau} = \sqrt{\left(\frac{t_b}{2}\right)^2 + \frac{\sigma^2_{\{t_i<T\}}}{N} + \left(\frac{Mt_b N_0}{N^2}\right)^2 \frac{N(N_0 - N)}{N_0}} = \sqrt{\left(\frac{t_b}{2}\right)^2 + \frac{\sigma^2_{\{t_i<T\}}}{N} + \left(\frac{Mt_b}{N}\right)^2 N_0(\frac{N_0}{N} - 1)}. \quad (46)$$

Here the fluctuations in the average accepted times are assumed independent from the fluctuations in the number of accepted events, and the number of accepted events is assumed to be drawn from a binomial

distribution. The probability of an event to be accepted (rejected) is $p = 1 - e^{-T/\tau}$ ($q = 1 - p$). The mean number of accepted events is $N = N_0 p$. The variance in number of accepted events is according to same distribution is $\mathrm{var}\{N\} = N_0 p(1-p) = N\frac{(N_0 - N)}{N_0}$. The analysis was done for acceptance windows of different lengths. The result is shown in figure 26.

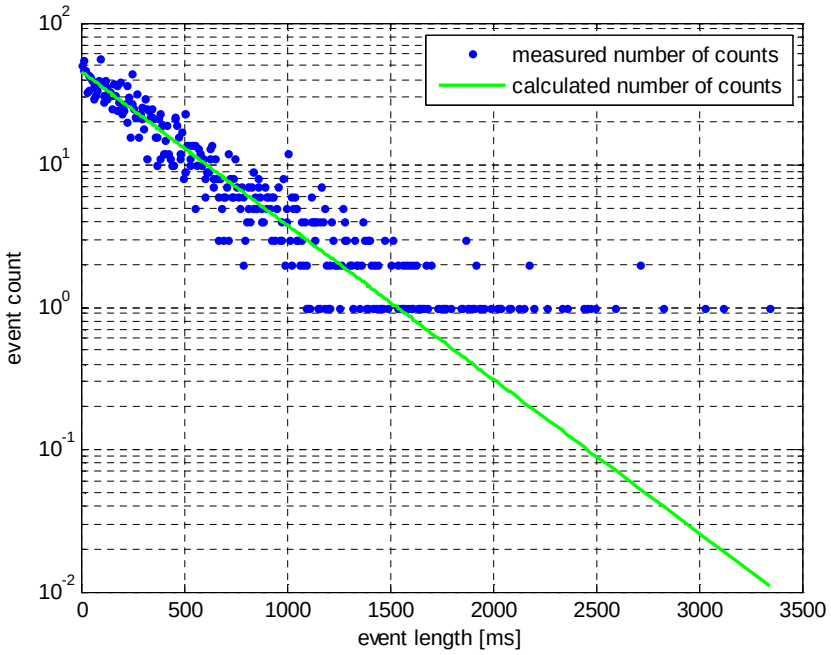

Figure 25: Histogram of measured decay times.
Filled circles are the actual measurements while the solid line is calculated for the estimated value for $\tau = 395 \pm 10\,\mathrm{ms}$.

Looking at the histogram in figure 25 we see that the frequency of counts at times larger than about 1500 ms ($\approx 3.5 \times \tau$) is higher than expected for an exponential decay with the measured lifetime. This we believe is due to reshelving of the ion during a measurement: because Raman pulses are present even when the ion is in the dark state, there is some probability for an ion to decay from the shelved state and be re-shelved during one bin. This will not be detected because this event will take place between detection pulses. A reshelving event serves to decrease the total number of counted events in a time bin which will tend to increase the mean time of dark events and the estimate of the lifetime. The way these reshelving events are treated in the analysis is by introducing a finite acceptance window. We only use events short enough so that reshelving events do not occur with high probability. The effect of including time bins that have more and more reshelving events is evident in figure 26. We see "jumps" in the estimated lifetime at acceptance window lengths of approximately 400 ms and 800 ms- close to one and two lifetimes. For the estimated lifetime we take the result just before the first such "jump"- $\hat{\tau} = 395 \pm 10\,\mathrm{ms}$.

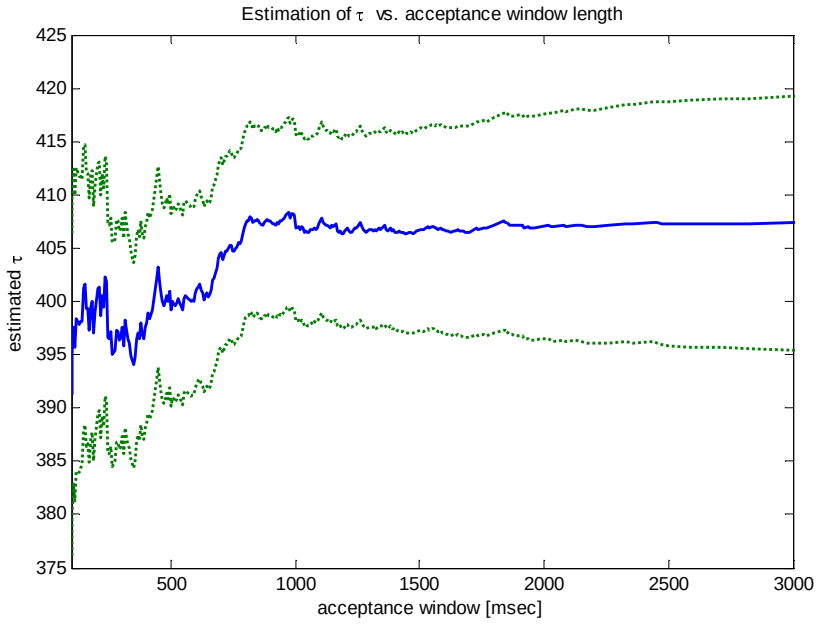

Figure 26: Maximum likelihood estimation for τ.
Maximum likelihood estimator with changing acceptance window length. The solid line is the estimation for τ while the area between the dashed lines gives the 1σ error bound for the estimation.

In figure 27 we plot past measured values of τ vs. the measurement year. In this work we measure a value in agreement with most of the previous results, specifically with the much more accurate result by NPL (2006): $\tau_{\mathrm{NPL}} = 390.8 \pm 1.6\,\mathrm{ms}$ [36].

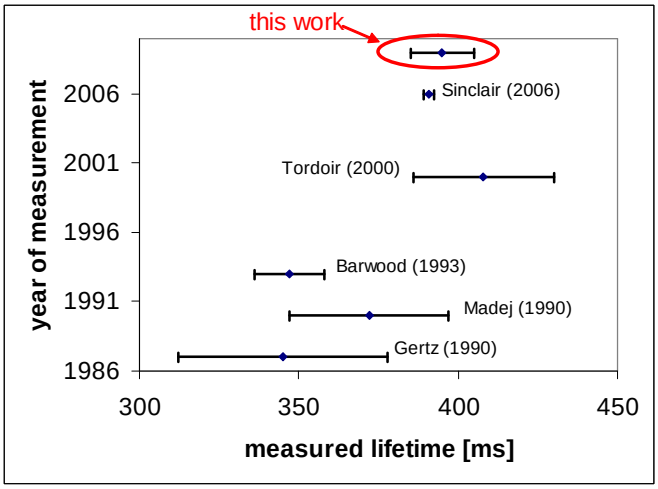

Figure 27: Past measurements of $4D_{\frac{5}{2}}$ lifetime.

4.2.3 Second Order Coherence of 674 nm Field

We can use the quantum jumps we observed to demonstrate photon anti-bunching in our system, i.e. the existence of a light field with second order coherence, $g^{(2)}(t) = \frac{\langle n(0)n(t)\rangle}{\langle n\rangle^2}$ that is smaller than unity as $t \to 0$. The second order coherence is the normalized auto-correlation function of the intensity. For classical fields the definition of intensity leads to $g^{(2)}(t) < g^{(2)}(0)$ and $g^{(2)}(0) > 1$, while for quantum fields, the definition of the intensity in terms of operators allows all possible values of $g^{(2)}(0)$. Therefore- an observation of $g^{(2)}(0)$<1 and more generally $g^{(2)}(0) < g^{(2)}(t > 0)$ is a clear signature of the quantum nature of the observed field [37].

Every time the meta-stable $4D_{\frac{5}{2}}$ decays into the Λ "state" a single 674nm photon is emitted. Since we detect those decay events with efficiency close to 100% (neglecting the rare multiple-decay, caused by reshelving) we know the time those 674 nm photons were emitted. By looking of the normalized mean number of 674 nm photons emitted at time t after a 674 nm photon is emitted, we can have a measurement of the second order coherence of the 674 nm field. The form of $g^{(2)}(t)$ is plotted in figure 28 and shows clear signature of photon anti-bunching: the probability to emit a 674 nm photon right after one was emitted is smaller than at later times. From the solution of rate equations for the Λ and $4D_{\frac{5}{2}}$ states, a theoretical prediction for $g^{(2)}$ is obtained, $g^{(2)} = 1 - e^{-(R+\gamma)t}$. Here R is the rate of quantum jumps (inverse of the mean time of bright periods) and $\gamma = 1/\tau$ is the lifetime of the metastable state .

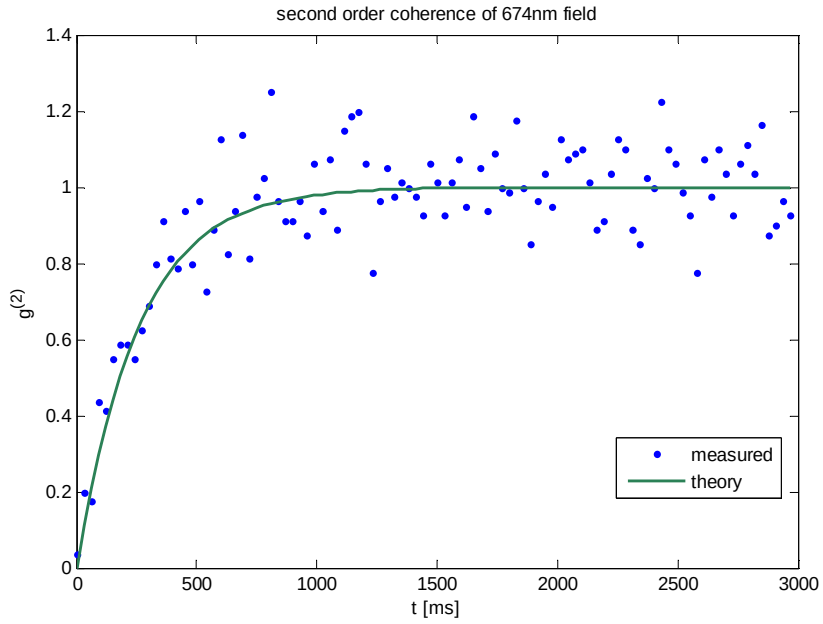

Figure 28: Second order coherence of 674 nm radiation.
Second order coherence of 674 nm radiation, deduced by observation of the decay times of the $4D_{\frac{5}{2}}$ metastable state. The theoretical curve, $g^{(2)} = 1 - e^{-(R+\gamma)t}$, is obtained from the solution of rate equations for the Λ and $4D_{\frac{5}{2}}$ states and treating the system as a two level system. Here R is the rate of quantum jumps (inverse of the mean time of bright periods) and $\gamma = 1/\tau$, where τ is the measured lifetime of the metastable state .

5 Conclusions

We have designed and built a laser system that will be used to perform single qubit gates on a trapped ion qubit with high fidelity. Not including errors originating from laser beam pointing instability on the ion we estimate that the classically contribution to the errors in the gate is lower than 10^{-7}. The gate will be therefore quantum noise limited, i.e. limited by the spontaneous scattering of photons from the ion with $\varepsilon_s = 8 \times 10^{-6}$ (for a 405.5 nm laser). The classical noises have been attenuated by the application of active feedback methods and utilize a field programmable gate array card. The laser was not tested on the ion since the state detection scheme was not yet fully implemented in the lab by the time this thesis was written.

Radiation at 408 nm present in the laser beam was detected by looking at indirect shelving of the ion in the $D_{\frac{5}{2}}$ metastable state and was attenuated to undetectable level by a filtering diffraction grating and a single-mode optical fiber.

It is planned to measure the fidelity of the rotation gate by the methods outlined in [8]. When the

final stage of the project will be successfully implemented, we will have demonstrated a single qubit gate of fidelity exceeding the fidelity required for quantum error correction and fault tolerant quantum computing.

Further work is probably needed to obtain the desired high fidelity gates. A better, more stable ECDL is being designed for use as the source of the Raman beams. It will utilize a stainless-steel commercial mirror mount with better thermal and mechanical stability than the apparatus we use now which was built in house and is made of Aluminum. The extended cavity will be made of Invar to further reduce thermally induced noises.

A Appendix

A.1 Calculating Electric Dipole Matrix Elements

When calculating the Rabi frequency of a Raman transition, we have to evaluate terms of the form $\langle Jm_f | er_{q_2} | J'm' \rangle \langle J'm' | er_{q_1} | Jm_i \rangle$, where the right matrix element is for the absorption process and the left one is for stimulated emission. Using the Wigner-Eckart theorem on the stimulated emission term we have

$$\langle Jm | er_q | J'm' \rangle = \langle J \| er \| J' \rangle \langle J' 1 m' q | Jm \rangle , \tag{47}$$

where $\langle J \| er \| J' \rangle$ is the reduced matrix element and $\langle J' 1 m' q | Jm \rangle$ is the appropriate CG coefficient. Using the identity[6],

$$\langle j_1 j_2 m_1 m_2 | j_1 j_2 jm \rangle = (-1)^{j+j_1-m-m_1} \sqrt{\frac{2j+1}{2j_1+1}} \langle j j_2 m\text{-}m_2 | j_1 m_1 \rangle , \tag{48}$$

to exchange between the initial and final total angular momentum ($J \leftrightarrow J'$), we get

$$\langle Jm | er_q | J'm' \rangle = \langle J \| er \| J' \rangle (-1)^{J+J'-m-m'} \sqrt{\frac{2J+1}{2J'+1}} \langle J\, 1 m\text{-}q | J'm' \rangle . \tag{49}$$

Taking the hermitian conjugate of the LHS:

$$\langle Jm | er_q | J'm' \rangle^\dagger = \langle J'm' | er_{-q} | Jm \rangle = \langle J' \| er \| J \rangle \langle J\, 1 m\text{-}q | J'm' \rangle , \tag{50}$$

and remembering that dipole matrix elements for between bound states are real we get

$$\langle J \| er \| J' \rangle (-1)^{J+J'-m-m'} \sqrt{\frac{2J+1}{2J'+1}} = \langle J' \| er \| J \rangle . \tag{51}$$

The $(-1)^{J+J'-m-m'}$ is just 1 for transitions with integer spin difference. We get that the reduced matrix element changes between absorption and emission (here J' is the higher energy level),

$$(2J'+1) \left| \langle J' \| er \| J \rangle \right|^2 = (2J+1) \left| \langle J \| er \| J' \rangle \right|^2 . \tag{52}$$

[6] http://functions.wolfram.com/07.38.17.0060.01

The reduced matrix element of the **emission** [22]:

$$\left|\left\langle J \left\| er \right\| J' \right\rangle\right|^2 = \frac{2J'+1}{2J+1} 3\pi\varepsilon_0\hbar\frac{c^3}{\omega_0^3}\frac{1}{\tau} \tag{53}$$

and for the **absorption** it is,

$$\left|\left\langle J' \left\| er \right\| J \right\rangle\right|^2 = 3\pi\varepsilon_0\hbar\frac{c^3}{\omega_0^3}\frac{1}{\tau}, \tag{54}$$

where τ is the lifetime of the excited level. Note that the degeneracy factor of $\frac{2J'+1}{2J+1}$ does not appear in this expression.

To conclude: when we need to evaluate terms like $\left\langle Jm_f \left| er_{q_2} \right| J'm' \right\rangle \left\langle J'm' \left| er_{q_1} \right| Jm_i \right\rangle$ we can make the job easier by taking the conjugate of the emission term, making it an absorption term with $q \to -q$. We can then use the simpler CG coefficient for absorption and need not pay attention for degeneracy factors and get

$$\left\langle Jm_f \left| er_{q_2} \right| J'm' \right\rangle \left\langle J'm' \left| er_{q_1} \right| Jm_i \right\rangle = 3\pi\varepsilon_0\hbar\frac{c^3}{\omega_0^3}\frac{1}{\tau}\left\langle J\,1m_f\text{-}q_2 | J'm' \right\rangle \left\langle J\,1m_i q_1 | J'm' \right\rangle$$

A.2 Modulated Laser Statistics

The voltage signal at the photo-detector output is given by $v(t) = G \times i(t) = G\frac{e}{T_d}N(t)$ where G is the trans-impedance gain of the detector amplifier, e is the electron charge, T_d is the time constant of the detector and $N(t)$ is the number of photons detected during time T_d. $N(t)$ is a Poissonian random number with rate $\eta T_d \Gamma(t)$ where η is the quantum efficiency of the detector and $\Gamma(t)$ is the time dependent rate of arrival of photons to the detector. When the laser intensity is modulated it is the rate of arrival of photons that depends on time. For example, simple amplitude modulation yields,

$$\Gamma(t) = \Gamma_0(1 + A_m \sin(\omega_m t)), \tag{55}$$

where $\Gamma_0 = \frac{P_0}{\hbar\omega_{laser}}$ is the average rate of photon arrival (P_0 is the average power in the beam), $0 \le A_m \le 1$ is the modulation amplitude and $\omega_m = 2\pi f_m$ is the modulation frequency. In the servo scheme used we measure the demodulated signal, which is obtained by mixing the detected signal with a local oscillator (LO) and low-pass-filtering the result. The mixed signal is given by $v_{IF}(t) = A_{LO}\sin(\omega_m t)v(t)$ where A_{LO} is the amplitude of the LO. In the frequency domain this signal has the form $V_{IF}(f) = \frac{1}{2i}A_{LO}(V(f-f_m) - V(f+f_m))$. The filtered signal is simply $V_{LP}(f) = H_{LP}(f)V_{IF}(f)$, where H_{LP} is the frequency response

of the low-pass filter (LPF). We first look at the mean demodulated signal for the simple modulation in Eq. (55):

$$\begin{aligned}\langle v_{LP}(t)\rangle = LPF\{\langle v(t)\rangle \cdot A_{LO}\sin(\omega_m t)\} = LPF\{G\langle i(t)\rangle \cdot A_{LO}\sin(\omega_m t)\} = \\ = LPF\{G\frac{e}{T_d}\langle N(t)\rangle \cdot A_{LO}\sin(\omega_m t)\} = \\ = LPF\{G\frac{e}{T_d}\eta T_d \Gamma_0(1+A_m\sin(\omega_m t))\cdot A_{LO}\sin(\omega_m t)\} =, \\ = Ge\eta\Gamma_0\frac{A_m A_{LO}}{2} = \frac{A_m A_{LO}}{2}v_{DC}. \quad (56)\end{aligned}$$

$Ge\eta\Gamma_0 = v_{DC}$ is the measured voltage zero modulation, $A_m = 0$. We are interested in the auto-covariance function of the demodulated noise: $C_{LP}(t_1,t_2) = \langle \Delta v_{LP}(t_1)\Delta v^*_{LP}(t_2)\rangle$ where $\Delta x(t) = x(t) - \langle x(t)\rangle$. The auto-covariance function can be written in terms of the Fourier transforms

$$\begin{aligned}C_{LP}(t_1,t_2) = \left\langle \int df_1 e^{-i2\pi f_1 t_1}\Delta V_{LP}(f_1)\int df_2 e^{i2\pi f_2 t_2}\Delta V^*_{LP}(f_2)\right\rangle = \\ \int df_1\int df_2 e^{-i2\pi(f_1 t_1 - f_2 t_2)}\frac{1}{4}A^2_{LO}H_{LP}(f_1)H^*_{LP}(f_2)\langle(\Delta V(f_1-f_m)-\Delta V(f_1+f_m))(\Delta V^*(f_2-f_m)-\Delta V^*(f_2+f_m))\rangle. \quad (57)\end{aligned}$$

We need to evaluate terms of the form $\langle \Delta V(f_1)\Delta V^*(f_2)\rangle$. To do this we transform again to the time domain,

$$\langle \Delta V(f_1)\Delta V^*(f_2)\rangle = \int dt_1\int dt_2 e^{-i2\pi(f_1 t_1 - f_2 t_2)}\langle \Delta V(t_1)\Delta V(t_2)\rangle \quad (58)$$

with $\Delta V(t) = G\frac{e}{T_d}\Delta N(t)$. Due to separation of timescales (the detector is fast w.r.t. the modulation frequency and the LP filter, i.e. $T_d \ll \frac{2\pi}{\omega_m}$, $T_d \ll \frac{2\pi}{\omega_{LP}}$) the auto-covariance of the photon number can be approximated by $\langle \Delta N(t_1)\Delta N(t_2)\rangle \approx T_d\langle N(t_1)\rangle\delta(t_1-t_2) = \eta T_d^2\Gamma(t_1)\delta(t_1-t_2)$ (see page 390 of [25]). Where in the first step the Poissonian nature of $N(t)$ is used. We then get

$$\begin{aligned}\langle \Delta V(f_1)\Delta V^*(f_2)\rangle = G^2e^2\eta\int dt_1\int dt_2 e^{-i2\pi(f_1 t_1 - f_2 t_2)}\Gamma(t_1)\delta(t_1-t_2) = \\ = G^2e^2\eta\int dt_1 e^{-i2\pi(f_1-f_2)t_1}\Gamma(t_1) \equiv G^2e^2\eta\hat{\Gamma}(f_1-f_2). \quad (59)\end{aligned}$$

The expression for the auto-correlation function contains three terms of this form. These are

$$G^2e^2\eta\left(2\hat{\Gamma}(f_1-f_2)-\hat{\Gamma}(f_1-f_2-2f_m)-\hat{\Gamma}(f_1-f_2+2f_m)\right). \quad (60)$$

With $\hat{\Gamma}(f) = \Gamma_0 (\delta(f) + A_m \delta(f - f_m))$ (the fourier transform of Eq. (55)) and assuming that the LP filter, H_{LP}, is chosen to reject f_m, the only term contributing in (57) is $2\hat{\Gamma}(f_1 - f_2)$ and the other two are rejected by the LP filter. We end up with

$$C_{LP}(t_1, t_2) = \frac{1}{2} A_{LO}^2 G^2 e^2 \eta \Gamma_0 \int df_1 e^{-i2\pi(t_1 - t_2)f_1} |H_{LP}(f_1)|^2 \tag{61}$$

and we immediately get the power spectrum of the noise signal $S(f) = \frac{1}{2} A_{LO}^2 G^2 e^2 \eta \Gamma_0 |H_{LP}(f)|^2 = \frac{1}{2} A_{LO}^2 G e v_{DC} |H_{LP}(f)|^2$ where in the last step we recognize the DC voltage seen on the detector as $v_{DC} = G i_{DC} = G e \eta \Gamma_0$. We note that since $C_{LP}(t_1, t_2) = C_{LP}(t_1 - t_2)$ (the noise auto-correlation function only depends on the time difference) the noise is stationary, and it resembles a white noise process in the BW of the LP filter.

We repeat the derivation the case of unmodulated beam ($A_m = 0$), and detection voltage signal $v(t)$ passed through the same low pass filter H_{LP}, result in $v'_{LP}(t)$. This time no mixing-down of the signal is required. The auto-covariance is again

$$C'_{LP}(t_1, t_2) = \left\langle \int df_1 e^{-i2\pi f_1 t_1} \Delta V'_{LP}(f_1) \int df_2 e^{i2\pi f_2 t_2} \Delta V^*_{LP}(f_2) \right\rangle,$$

and we get a power spectrum $S'(f) = G e v_{DC} |H_{LP}(f)|^2$. This is the same power spectrum obtained for the modulated-then-demodulated noise, without the prefactor $\frac{A_{LO}^2}{2}$ which is the result of the mix-down process.

References

[1] Nielsen, M. A. and Chuang, I. L. *Quantum Computation and Quantum Information*. Cambridge University Press, October (2000).

[2] Feynman, R. *International Journal of Theoretical Physics* **21**(6), 467–488 June (1982).

[3] Shor, P. W. , 124–134 (1994).

[4] Shor, P. W. *SIAM Journal on Computing* **26**, 1484–1509 (1997).

[5] Barenco, A., Bennett, C. H., Cleve, R., DiVincenzo, D. P., Margolus, N., Shor, P., Sleator, T., Smolin, J. A., and Weinfurter, H. *Phys. Rev. A* **52**(5), 3457–3467 Nov (1995).

[6] Shannon, C. E. (1948).

[7] Divincenzo, D. P. *Fortschritte der Physik* **48**(9-11), 771–783 (2000).

[8] Knill, E., Leibfried, D., Reichle, R., Britton, J., Blakestad, R. B., Jost, J. D., Langer, C., Ozeri, R., Seidelin, S., and Wineland, D. J. *Physical Review A (Atomic, Molecular, and Optical Physics)* **77**(1), 012307 (2008).

[9] Myerson, A. H., Szwer, D. J., Webster, S. C., Allcock, D. T. C., Curtis, M. J., Imreh, G., Sherman, J. A., Stacey, D. N., Steane, A. M., and Lucas, D. M. *Physical Review Letters* **100**(20), 200502 (2008).

[10] Langer, C. E. *High Fidelity Quantum Information Processing with Trapped Ions*. PhD thesis, University of Colorado, (2006).

[11] Langer, C., Ozeri, R., Jost, J. D., Chiaverini, J., DeMarco, B., Ben-Kish, A., Blakestad, R. B., Britton, J., Hume, D. B., Itano, W. M., Leibfried, D., Reichle, R., Rosenband, T., Schaetz, T., Schmidt, P. O., and Wineland, D. J. *Phys. Rev. Lett.* **95**(6), 060502 Aug (2005).

[12] Leibfried, D., Demarco, B., Meyer, V., Lucas, D., Barrett, M., Britton, J., Itano, W. M., Jelenkovic, B., Langer, C., Rosenband, T., and Wineland, D. J. *Nature* **422**(6930), 412–415 March (2003).

[13] Paul, W. *Rev. Mod. Phys.* **62**(3), 531–540 Jul (1990).

[14] Wineland, D. J., Monroe, C., Itano, W. M., Leibfried, D., King, B. E., and Meekhof, D. M. *J.RES.NATL.INST.STAND.TECH.* **103**, 259 (1998).

[15] Leibfried, D., Blatt, R., Monroe, C., and Wineland, D. *Rev. Mod. Phys.* **75**(1), 281–324 Mar (2003).

[16] Itano, W. M., Bergquist, J. C., Bollinger, J. J., and Wineland, D. J. *Proc. 1991 Laser Manipulation of Atoms and Ions Conf.* , 519–537 (1991).

[17] Itano, W. M. and Wineland, D. J. *Phys. Rev. A* **25**(1), 35–54 Jan (1982).

[18] Ozeri, R., Itano, W. M., Blakestad, R. B., Britton, J., Chiaverini, J., Jost, J. D., Langer, C., Leibfried, D., Reichle, R., Seidelin, S., Wesenberg, J. H., and Wineland, D. J. *Physical Review A (Atomic, Molecular, and Optical Physics)* **75**(4) (2007).

[19] Wineland, D. J., Barrett, M., Britton, J., Chiaverini, J., Demarco, B., Itano, W. M., Jelenković, B., Langer, C., Leibfried, D., Meyer, V., Rosenband, T., and Schätz, T. *Philosophical Transactions: Mathematical, Physical and Engineering Sciences* **361**(1808), 1349–1361 (2003).

[20] Cirac, J. I. and Zoller, P. *Physical Review Letters* **74**(20), 4091 May (1995).

[21] Lambropoulos, P. and Petrosyan, D. *Fundamentals of Quantum Optics and Quantum Information*. Springer-Verlag New York, Inc., Secaucus, NJ, USA, (2006).

[22] Steck, D. A. *available online at http://steck.us/alkalidata.* (2008).

[23] Sakurai, J. J. *Modern Quantum Mechanics (2nd Edition)*. Addison Wesley, January (1994).

[24] Mollow, B. R. *Physical Review A* **12**(5), 1919 November (1975).

[25] Papoulis, A. and Pillai, U. S. *Probability, Random Variables and Stochastic Processes*. McGraw-Hill Science/Engineering/Math, December (2001).

[26] Goren Gordon, N. E. and Kurizki, G. *Journal of Physics B: Atomic, Molecular and Optical Physics* **40**, S75–S93 (2007).

[27] Ozeri, R., Langer, C., Jost, J. D., DeMarco, B., Ben-Kish, A., Blakestad, B. R., Britton, J., Chiaverini, J., Itano, W. M., Hume, D. B., Leibfried, D., Rosenband, T., Schmidt, P. O., and Wineland, D. J. *Phys. Rev. Lett.* **95**(3), 030403 Jul (2005).

[28] Ludlow, A. D., Huang, X., Notcutt, M., Zanon-Willette, T., Foreman, S. M., Boyd, M. M., Blatt, S., and Ye, J. *Opt. Lett.* **32**(6), 641–643 (2007).

[29] Vant, K., Chiaverini, J., Lybarger, W., and Berkeland, D. J. (2006).

[30] Ricci, L., Weidemüller, M., Esslinger, T., Hemmerich, A., Zimmermann, C., Vuletic, V., König, W., and Hänsch, T. W. *Optics Communications* **117**(5-6), 541 – 549 (1995).

[31] Lenstra, D., Verbeek, B., and Den Boef, A. *Quantum Electronics, IEEE Journal of* **21**(6), 674–679 Jun (1985).

[32] Bachor, H.-A. *A guide to experiments in quantum optics / Hans-A. Bachor*. Wiley-VCH, Weinheim ; New York :, (1998).

[33] Robertson, N. A., Hoggan, S., Mangan, J. B., and Hough, J. *Applied Physics B-photophysics and Laser Chemistry* **39**(3), 149–153 March (1986).

[34] Oppenheim, A. V., Schafer, R. W., and Buck, J. R. *Discrete-Time Signal Processing (2nd Edition)*. Prentice Hall, February (1999).

[35] Hobbs, P. C. D. *Building Electro-Optical Systems, Making it All Work*. (2000).

[36] Letchumanan, V. ; Wilson, M. A. . G. P. and Sinclair, A. G. *Phys. Rev. A* **72**(1), 012509 Jul (2005).

[37] Loudon, R. *The Quantum Theory of Light (Oxford Science Publications)*. OUP Oxford, 3 edition, September (2000).